POLITECNICO
MILANO 1863

SCUOLA DI INGEGNERIA INDUSTRIALE
E DELL'INFORMAZIONE

Development and characterization of a hybrid time-resolved reflectance spectroscopy and diffuse correlation spectroscopy system for hemodynamic and metabolic measurements

Tesi di Laurea Magistrale in
Engineering Physics – Ingegneria Fisica

Author: **Marco Nabacino**

Student ID: 962836
Advisor: Prof. Alessandro Torricelli
Co-advisor: Caterina Amendola, PhD
Academic Year: 2021-22

"If we knew what it was we were doing,
it would not be called research,
would it?"

– Albert Einstein

Acknowledgements

I wish to thank my advisor, Prof. Alessandro Torricelli, for giving me the opportunity to attend the research laboratories at the Department of Physics of Politecnico di Milano and for offering precious advice during my thesis work.

A special thank to my co-advisor, Dr. Caterina Amendola, for her constant and competent support and for being always available in every step of my work. She provided her valuable experience and guidance throughout the experimental activities and the composition of this thesis.

Abstract

The work developed in this thesis concerns the design and characterization of an innovative hybrid TRS and DCS instrument for hemodynamic and metabolic measurements. TRS and DCS are diffuse optics techniques that make use of infrared laser light in order to probe biological tissue in a non-invasive manner. More specifically, TRS gives information on the components of a tissue along with their concentration, while DCS allows to quantify blood flow. The combination of the two thus allows a comprehensive all-optical measurement of tissue oxygenation and hemodynamics. The TRS module makes use of a state-of-the-art TD-NIRS system employing two wavelengths and featuring two detection channels, which enables to separate between the contributions of superficial and deep tissue. It was characterized in terms of stability as well as linearity and accuracy against a previously built and validated instrument, showing that it is suitable for both absolute and relative measurements. The DCS module similarly features multiple detection channels and makes use of a software autocorrelator, which gives more flexibility compared to its hardware counterparts. Different autocorrelation algorithms were investigated in terms of time performance, stability and capability of following variations of experimental parameters. This allowed to identify the best options both for real-time measurements and post-processing.

Keywords: diffuse correlation spectroscopy; near-infrared spectroscopy; diffuse optics; photon migration; correlators

Abstract in lingua italiana

Il lavoro affrontato in questa tesi riguarda la progettazione e caratterizzazione di un innovativo dispositivo ibrido TRS e DCS per misure emodinamiche e metaboliche. TRS e DCS sono tecniche di ottica diffusiva che impiegano luce laser infrarossa per sondare tessuti biologici in maniera non invasiva. Più precisamente, TRS dà informazioni sulle componenti di un tessuto e la loro concentrazione, mentre DCS permette di quantificare il flusso sanguigno. La combinazione delle due tecniche permette perciò una misura completa interamente ottica dell'ossigenazione e dell'emodinamica di un tessuto. Il modulo TRS impiega un sistema TD-NIRS allo stato dell'arte che fa uso di due lunghezze d'onda e due canali di rilevazione, i quali permettono di separare i contributi degli strati di tessuto superficiali da quelli degli strati profondi. È stato caratterizzato in termini di stabilità così come linearità e accuratezza rispetto a uno strumento precedentemente costruito e validato, mostrando che è adatto sia per misure assolute che relative. Il modulo DCS analogamente possiede diversi canali di rilevazione e impiega un autocorrelatore software, che offre maggiore flessibilità rispetto alle sue controparti hardware. Sono stati investigati diversi algoritmi di autocorrelazione in termini di velocità, stabilità e capacità di seguire variazioni di parametri sperimentali. Ciò ha permesso di individuare le opzioni migliori sia per misure in tempo reale che per elaborazione dati in post-processing.

Parole chiave: spettroscopia diffusiva di correlazione; spettroscopia nel vicino infrarosso; ottica diffusiva; migrazione di fotoni; correlatori

Contents

Introduction

"Everything is interesting if you go into it deeply enough"
– Richard Feynman

The idea of using light in the biomedical field is everything but new: for example, 90 years ago it was used to see tumors in thick tissues [1]. Optical techniques for imaging and diagnostic are particularly attractive due to them being non-invasive while still being able to investigate several centimeters deep into the tissue [2]. This is made possible by the employment of near-infrared (NIR) light, which as shown in fig. 1 is absorbed relatively little in the $650 \div 950$ nm range.

As light propagates through biological tissues it is both absorbed and scattered, with the latter phenomenon being prevalent. Absorption is tied to which molecules are present in the medium as well as their concentration, while scattering to their geometry and distribution. The basic idea of diffuse optics techniques is to collect the photons that have interacted with the sample in order to obtain information on the sample itself. Three types of light sources are commonly employed (fig. 2):

Continuous-Wave (CW) sources are the simplest ones, emitting light with constant intensity. After propagating through the medium, the detected light's intensity is likewise constant, and by measuring its attenuation it is possible to gain information on the investigated sample. CW techniques allow fast data acquisition and simple detection systems, but have the major drawback of not being able to differentiate between absorption and scattering.

Intensity-modulated sources are more complex than CW ones, but also allow to gain more information. They are employed for frequency-domain (FD) experiments, in which the light intensity of the source oscillates in time (with angular frequency of order $100\,\text{MHz} \div 1\,\text{GHz}$): the collected light's intensity also oscillates at the same frequency, but with different amplitude and phase. By measuring these last two quantities it is possible to separate the contributions of absorption and scattering.

Pulsed sources emit short light pulses ($< 100\,\text{ps}$) that after propagating through the tissue become broadened and attenuated. Time-domain (TD) approaches in principle

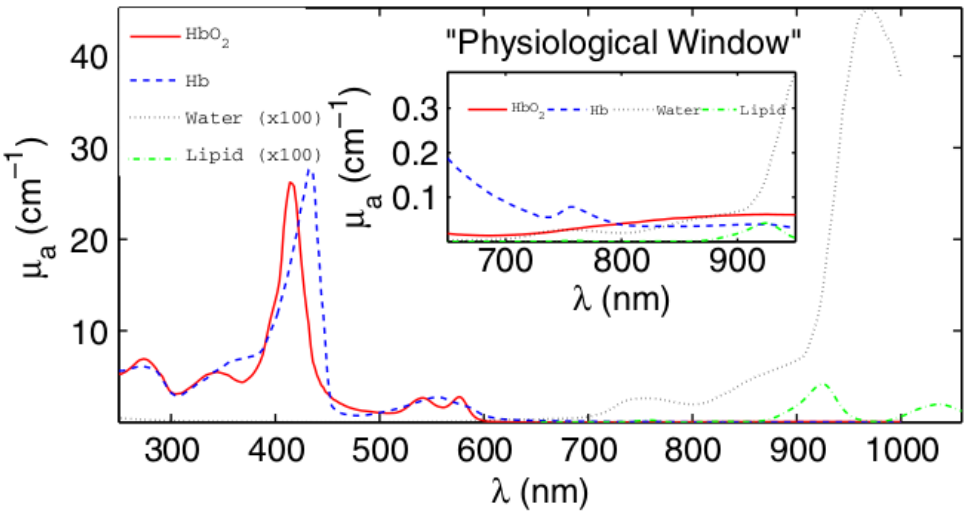

Figure 1: Absorption spectra of the main components of biological tissue. In the so-called *physiological window* water, lipid and hemoglobin absorptions are relatively low. From [2].

convey the same amount of information as FD ones, since the two are related mathematically via a Fourier transform. Additionally, techniques such as time-gating allow to pathlength-resolve the detected photons to separate the contributions of different layers of tissue.

Perhaps the best-known family of diffuse optics techniques is near-infrared spectroscopy (NIRS). NIRS allows to measure the tissue optical parameters and to retrieve from them oxy- and deoxy-hemoglobin, water and lipid concentrations through their absorption spectra. Applications of this technique include brain monitoring [3] and muscles oxidative metabolism assessment [4], but NIRS also allows optical imaging, which has been

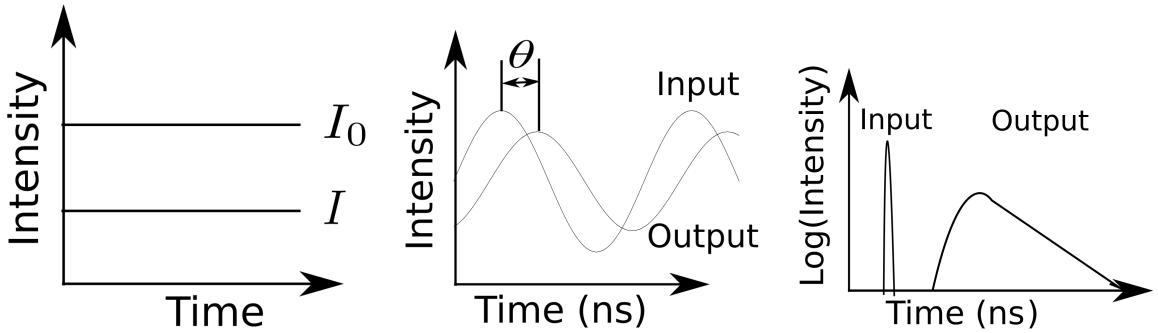

(a) Continuous Wave (CW) (b) Frequency Domain (FD) (c) Time Domain (TD)

Figure 2: Summary of the signals measured in different diffuse optics approaches (adapted from [2])

harnessed to investigate brain functional activation during cognitive and somatosensory tasks [5] and for spectroscopic tumor characterization [6].

Another diffuse optics technique that has been gaining increasing interest in recent years is diffuse correlation spectroscopy (DCS). DCS exploits long-coherence laser light that gets scattered by moving particles (red blood cells in biological tissue) and generates at the detection plane a speckle interference pattern that fluctuates in time. By measuring the temporal evolution of the intensity and calculating its autocorrelation, DCS allows to obtain information on the movement of red blood cells. Since this technique is based on physical principles that are very similar to NIRS, the two share the same advantages, such as non-invasiveness, deep penetration and excellent temporal resolution [7].

DCS has been extensively validated *in vivo* against established techniques such as Doppler ultrasound and MRI, showing that it is able to determine relative changes of tissue blood flow quite well with respect to a baseline [7]. Examples of applications of DCS include assessment of cerebral autoregulation in ischemic stroke patients [8] and continuous monitoring of cerebral blood flow in comatose patients [9], but its range of applications goes beyond the brain, including contexts such as cancer and peripheral arterial disease [7].

In order to obtain information on blood flow from DCS, tissue optical parameters must be measured first [7], a task that is readily fulfilled by NIRS. As such, incorporating in the same instrument NIRS and DCS allows to make comprehensive all-optical hemodynamic and metabolic measurements. Moreover, the joint use of both techniques allows to measure quantities that each single technique is not able to retrieve on its own. An example of this is the cerebral metabolic rate of oxygen consumption ($CMRO_2$) [10], whose estimation requires fewer approximations when using both NIRS and DCS than it does when employing NIRS alone [2].

In this thesis the development and characterization of one such hybrid TD-NIRS and CW-DCS instrument is presented. Its performances were assessed in terms of stability, linearity, accuracy, precision, and effect of varying source-detector separation. Additionally, several different algorithms for calculating the autocorrelation of the DCS intensity fluctuations were compared in terms of speed, precision and accuracy.

1 | Theoretical basis

"All models are wrong, some are useful"
– George Box

In this chapter the physical background of time-domain reflectance spectroscopy (TRS) and diffuse correlation spectroscopy (DCS) will be presented. In particular, after discussing the basics of light interaction with turbid media, the physical models adopted to describe photon migration in biological tissue will be illustrated.

1.1. Light interaction with turbid media

As far as light propagation is concerned, biological tissue falls into the category of *turbid media,* that is, media which both absorb and scatter light propagating through them [11]. In a turbid medium several particles of varying size and refractive indices are suspended in a background: this spatially varying distribution of size and refractive indices gives rise to scattering [12]. On top of this, some amount of absorption will be present as well, due to excitation of the molecules in the tissue [11].

In this section a simple quantitative model for absorption and scattering will be illustrated, introducing some fundamental physical quantities.

1.1.1. Absorption

Absorption of light in an optical medium can be modelled in a heuristic way through the concept of *absorption cross section.* Whenever light impinges on an absorbing particle, only part of its intensity is absorbed, while the rest is transmitted. However, we can instead model the absorber as a smaller particle which completely blocks all the light it intercepts. The geometrical cross section of the particle in this equivalent description is called the absorption cross section σ_a.

Let's now consider a beam of light propagating through an optical medium made of several absorbers whose volumetric density is ρ_a. Indicating with S the transverse area of the

medium, a slice of thickness $\mathrm{d}z$ contains $\mathrm{d}N$ absorbers, with $\mathrm{d}N$ given by:

$$\mathrm{d}N = \rho_a S \, \mathrm{d}z$$

When light propagates through one such slice, the fraction of intensity I that gets absorbed is equal to the fraction of surface area that absorbs radiation:

$$\frac{\mathrm{d}I}{I} = -\frac{\sigma_a \mathrm{d}N}{S} = -\rho_a \sigma_a \, \mathrm{d}z$$

where the negative sign indicates that light is lost during propagation. Integrating this equation, we get *Lambert's law* for absorption:

$$I(z) = I(0) e^{-\mu_a z} \tag{1.1}$$

In eq. (1.1) we have introduced the *absorption coefficient* μ_a, defined by:

$$\mu_a = \rho_a \sigma_a$$

As can be easily seen, μ_a has the dimension of the reciprocal of a length, and in biological tissue typical values of this quantity for visible/NIR light are of the order of $0.1\,\mathrm{cm}^{-1}$. The reciprocal of the absorption coefficient is called *absorption mean free path,* and represents the average distance travelled by a photon before being absorbed [13]:

$$\ell_a = \frac{1}{\mu_a}$$

When many different absorbing substances (also called *chromophores)* are present, the total absorption coefficient can be calculated as the sum of the absorption coefficients of each chromophore [14]:

$$\mu_a = \sum_i \mu_{a,i} = \sum_i \rho_{a,i} \, \sigma_{a,i} \tag{1.2}$$

Equation (1.2), known as *Beer's law* for absorption, assumes that the different chromophores do not interact with one another. Of course, this hypothesis is not valid in general, and the Beer-Lambert law is bound to fail in some cases, such as high absorption or uneven distribution of chromophores [15].

1.1.2. Scattering

Scattering in turbid media can be modelled in a totally analogous way to absorption: as light propagates through a scattering medium, its intensity follows Lambert's law:

$$I(z) = I(0)e^{-\mu_s z} \tag{1.3}$$

It should be noted however that eq. (1.3) only holds when $\mu_s z \ll 1$, a condition known as *single-scattering regime*. The *scattering coefficient* μ_s is given by:

$$\mu_s = \sum_i \rho_{s,i}\, \sigma_{s,i} \tag{1.4}$$

where $\rho_{s,i}$ and $\sigma_{s,i}$ are the volumetric density and scattering cross-section of scatterer i, respectively.

A fundamental quantity for modelling scattering is the so-called *scattering phase function* $p(\hat{\boldsymbol{s}}, \hat{\boldsymbol{s}}')$, defined as the probability that a photon initially travelling along direction $\hat{\boldsymbol{s}}$ be scattered within the unit solid angle around direction $\hat{\boldsymbol{s}}'$. For isotropic scattering (scattering by spherical particles or randomly oriented non-spherical ones) the phase function only depends on the angle θ between $\hat{\boldsymbol{s}}$ and $\hat{\boldsymbol{s}}'$: $p(\hat{\boldsymbol{s}}, \hat{\boldsymbol{s}}') = p(\theta)$.

Being a probability density function, a normalization condition holds for p:

$$\int_{4\pi} p(\hat{\boldsymbol{s}}, \hat{\boldsymbol{s}}')\, \mathrm{d}\Omega' = 2\pi \int_0^\pi p(\theta) \sin\theta\, \mathrm{d}\theta = 1$$

When propagation is dominated by scattering, a single number is sufficient to characterize p: the *anisotropy factor* g, defined as the average cosine of the scattering angle [11]:

$$g = \langle \cos\theta \rangle = 2\pi \int_0^\pi \cos\theta\, p(\theta) \sin\theta\, \mathrm{d}\theta \tag{1.5}$$

The anisotropy factor gives information on the preferred direction of scattering: for example, when $g \simeq 1$ scattering occurs mainly in the forward direction, while for $g \simeq -1$ backward scattering is prevalent. As such, after just a single scattering event the radiation is not isotropic. Thus, an important parameter to characterize scattering is the *reduced scattering coefficient* $\mu_s' = \mu_s(1-g)$, whose reciprocal is called *transport mean free path* and represents the average distance a photon must travel before losing information on the original direction of propagation due to scattering events [13]:

$$\ell' = \frac{1}{\mu_s'} = \frac{1}{\mu_s(1-g)}$$

Typical values of g in biological tissue are around $0.8 \div 0.9$, while $\mu_s' \sim 10\,\mathrm{cm}^{-1}$.

Conversely to absorption, which depends on the chemical composition of the turbid medium, scattering depends on refractive index mismatch between the background and the scatterers, their geometry (size and shape), and the wavelength of the radiation [11]. In particular, two main scattering regimes can be identified:

- When the particles are small ($r/\lambda \leq 0.05$ [16]), we speak of Rayleigh scattering. In this regime the scattering coefficient strongly depends on the wavelength of the radiation: $\mu_s \propto \lambda^{-4}$. On the other hand, the phase function does not depend on λ at all, and is simply given by:

$$p(\theta) = \frac{3}{16\pi}(1 + \cos^2\theta)$$

  The asymmetry factor is $g = 0$ even if scattering is not isotropic.

- For large particles ($r \gg \lambda$), the scattering coefficient is almost independent of the size, whereas the phase function strongly depends on it. In particular, for bigger particles p becomes more forward peaked ($p(\theta = 0)$ increases), but the total power scattered in the forward direction ($\theta < \pi/2$) remains approximately constant, so that g does not change by much and its value depends instead on the relative refractive index between background and scatterers [16].

1.2. Photon migration through turbid media

In this section the mathematical model of the Radiative Transfer Equation (RTE) will be presented, together with its Diffusion Approximation. The RTE represents a heuristic way of modelling energy transport through a tissue, and is not rigorously derived from Maxwell's Equations. Nevertheless, it leads to useful models for many practical problems [17].

1.2.1. Quantities used to describe radiative transfer

The main quantity used to describe photon migration through turbid media is the *radiance* I, defined as follows: $I(\boldsymbol{r}, \hat{\boldsymbol{s}}, t)$ is the average power that at position $\boldsymbol{r}$ and time t flows through the unit area oriented in the direction of the unit vector $\hat{\boldsymbol{s}}$, due to photons moving within the unit solid angle around $\hat{\boldsymbol{s}}$ [11]. In other words, the power d^2P that at time t flows within the solid angle $\mathrm{d}\Omega$ through the elementary area $\mathrm{d}\Sigma$ oriented along $\hat{\boldsymbol{n}}$ placed

at $\boldsymbol{r}$ is given by:

$$\mathrm{d}^2P = I(\boldsymbol{r}, \hat{\boldsymbol{s}}, t)|\hat{\boldsymbol{n}} \cdot \hat{\boldsymbol{s}}|\mathrm{d}\Sigma\mathrm{d}\Omega$$

Another important quantity is the *fluence rate* (or simply *fluence)* Φ, defined as the integral of the radiance over the solid angle Ω:

$$\Phi(\boldsymbol{r}, t) = \int_{4\pi} I(\boldsymbol{r}, \hat{\boldsymbol{s}}, t)\,\mathrm{d}\Omega \tag{1.6}$$

Dividing the fluence by the speed of photons inside the medium v, one gets the energy density. Thus, the quantity:

$$U(\boldsymbol{r}, t) = \frac{\Phi(\boldsymbol{r}, t)}{vh\nu}$$

where h is Planck's constant and ν the frequency of light, represents the photon density at position $\boldsymbol{r}$ and time t. The fluence is therefore proportional to the number of photons per unit volume present in the medium.

Finally, the *flux vector* $\boldsymbol{J}$ is defined as:

$$\boldsymbol{J}(\boldsymbol{r}, t) = \int_{4\pi} I(\boldsymbol{r}, \hat{\boldsymbol{s}}, t)\hat{\boldsymbol{s}}\,\mathrm{d}\Omega \tag{1.7}$$

and represents the net flux of power, in both amount and direction.

1.2.2. The Radiative Transfer Equation

The RTE is an integro-differential equation that represents the energy balance for light propagating through a medium. In the more general case, it assumes the form [11]:

$$\begin{aligned}\frac{1}{v}\frac{\partial}{\partial t}I(\boldsymbol{r}, \hat{\boldsymbol{s}}, t) = &- \hat{\boldsymbol{s}} \cdot \boldsymbol{\nabla}[I(\boldsymbol{r}, \hat{\boldsymbol{s}}, t)] - (\mu_a + \mu_s)I(\boldsymbol{r}, \hat{\boldsymbol{s}}, t) \\ &+ \mu_s \int_{4\pi} p(\hat{\boldsymbol{s}}, \hat{\boldsymbol{s}}')I(\boldsymbol{r}, \hat{\boldsymbol{s}}', t)\,\mathrm{d}\Omega' + \varepsilon(\boldsymbol{r}, \hat{\boldsymbol{s}}, t)\end{aligned} \tag{1.8}$$

where $\mathrm{d}\Omega'$ is the unit solid angle around direction $\hat{\boldsymbol{s}}'$ and $\varepsilon(\boldsymbol{r}, \hat{\boldsymbol{s}}, t)$ represents the source term, that is, the power emitted at time t per unit volume and solid angle around $\hat{\boldsymbol{s}}$.

Considering the volume element $\mathrm{d}V$ around position $\boldsymbol{r}$, the various terms have a clear physical meaning:

- $\frac{1}{v}\frac{\partial}{\partial t}I(\boldsymbol{r}, \hat{\boldsymbol{s}}, t)\mathrm{d}V\mathrm{d}\Omega\mathrm{d}t$ is the total change of the energy propagating along $\hat{\boldsymbol{s}}$ within $\mathrm{d}V$, $\mathrm{d}\Omega$ and $\mathrm{d}t$. This term is null for steady-state sources [17].

- $-\hat{\boldsymbol{s}} \cdot \boldsymbol{\nabla}[I(\boldsymbol{r}, \hat{\boldsymbol{s}}, t)]\mathrm{d}V\mathrm{d}\Omega\mathrm{d}t$ is the energy loss due to propagation through $\mathrm{d}V$ along $\hat{\boldsymbol{s}}$, within $\mathrm{d}\Omega$ and $\mathrm{d}t$.
- $-(\mu_a + \mu_s)I(\boldsymbol{r}, \hat{\boldsymbol{s}}, t)\mathrm{d}V\mathrm{d}\Omega\mathrm{d}t$ is the fraction of energy propagating along $\hat{\boldsymbol{s}}$ within $\mathrm{d}V$, $\mathrm{d}\Omega$ and $\mathrm{d}t$ that is absorbed or scattered along a different direction.
- $\mu_s \int_{4\pi} p(\hat{\boldsymbol{s}}, \hat{\boldsymbol{s}}')I(\boldsymbol{r}, \hat{\boldsymbol{s}}', t)\,\mathrm{d}\Omega'\,\mathrm{d}V\mathrm{d}\Omega\mathrm{d}t$ is the energy coming from any direction $\hat{\boldsymbol{s}}'$ that gets scattered along direction $\hat{\boldsymbol{s}}$ within $\mathrm{d}V$, $\mathrm{d}\Omega$ and $\mathrm{d}t$.
- $\varepsilon(\boldsymbol{r}, \hat{\boldsymbol{s}}, t)\mathrm{d}V\mathrm{d}\Omega\mathrm{d}t$ is the energy generated inside $\mathrm{d}V$ along $\hat{\boldsymbol{s}}$ within $\mathrm{d}\Omega$ and $\mathrm{d}t$.

1.2.3. Diffusion Approximation for the RTE

Being an integro-differential equation, the RTE is difficult to solve as it appears in eq. (1.8) [18]. No general analytical solutions are available [19], so approximations that reduce it to an easier equation are usually employed. In particular, when scattering is prevalent over absorption ($\mu_s' \gg \mu_a$), the Diffusion Equation (DE) constitutes an approximation able to deliver accurate solutions while being easier to solve.

The Diffusion Approximation consists of the following two assumptions:

- The radiance inside a diffusive medium is almost isotropic. As a consequence, it can be expanded in the sum of an isotropic term and a linearly anisotropic one [11]:

$$I(\boldsymbol{r}, \hat{\boldsymbol{s}}, t) = \frac{1}{4\pi}\Phi(\boldsymbol{r}, t) + \frac{3}{4\pi}\boldsymbol{J}(\boldsymbol{r}, t) \cdot \hat{\boldsymbol{s}} \tag{1.9}$$

  Notice that, by the definition of fluence (eq. (1.6) on page 9), the first term represents the average radiance. Mathematically, eq. (1.9) represents a series development of the radiance in spherical harmonics, truncated at the second term [17], and represents a good approximation if the contribution of the higher-order harmonics is negligible.

  A similar development is employed for the source term as well:

$$\varepsilon(\boldsymbol{r}, \hat{\boldsymbol{s}}, t) = \frac{1}{4\pi}q_0(\boldsymbol{r}, t) + \frac{3}{4\pi}\boldsymbol{q_1}(\boldsymbol{r}, t) \cdot \hat{\boldsymbol{s}}$$

  where:

$$q_0(\boldsymbol{r}, t) = \int_{4\pi} \varepsilon(\boldsymbol{r}, \hat{\boldsymbol{s}}, t)\,\mathrm{d}\Omega \qquad \boldsymbol{q_1}(\boldsymbol{r}, t) = \int_{4\pi} \varepsilon(\boldsymbol{r}, \hat{\boldsymbol{s}}, t)\hat{\boldsymbol{s}}\,\mathrm{d}\Omega$$

- The diffuse flux vector $\boldsymbol{J}$ exhibits slow variations. More precisely, the variation of

the flux over a time range $\Delta t = 1/(v\mu_s')$ is negligible with respect to the value of the vector itself:

$$\frac{1}{v\mu_s'}\left|\frac{\partial \boldsymbol{J}(\boldsymbol{r},t)}{\partial t}\right| \ll |\boldsymbol{J}(\boldsymbol{r},t)|$$

As briefly mentioned, the previous assumptions hold true when photons undergo many scattering events, since these tend to randomize the direction of propagation, making the radiance almost isotropic. On the other hand, absorption hinders this effect, since it destroys photons before they have the chance to cover long path lengths.

Employing the Diffusion Approximation, the RTE simplifies to two separate equations for the fluence and the flux. For a homogeneous medium, the Diffusion Equation for the fluence assumes the form:

$$\left[\frac{1}{v}\frac{\partial}{\partial t} - D\nabla^2 + \mu_a\right]\Phi(\boldsymbol{r},t) = q_0(\boldsymbol{r},t) \tag{1.10}$$

while for the flux we get Fick's law:

$$\boldsymbol{J}(\boldsymbol{r},t) = -D\boldsymbol{\nabla}[\Phi(\boldsymbol{r},t)] \tag{1.11}$$

In eqs. (1.10) and (1.11) D is the *diffusion coefficient,* given by:

$$D = \frac{1}{3(\mu_a + \mu_s')} \simeq \frac{1}{3\mu_s'}$$

1.2.4. Solution of the Diffusion Equation

The DE can have many different solutions depending on the geometry of the problem. This is hardly surprising: being a differential equation, boundary conditions are needed. For our applications we are interested in the solution for the semi-infinite medium (a half-space), which will be obtained in this section.

In order to solve the DE in the semi-infinite case, it is convenient to first solve it for the infinite medium. It can be shown that, for a delta-like source positioned in the origin ($q_0(\boldsymbol{r},t) = Q_0\delta(\boldsymbol{r})\delta(t)$), the fluence in an infinite medium is [11]:

$$\Phi(\boldsymbol{r},t) = \frac{vQ_0}{(4\pi Dvt)^{3/2}}\exp\left(-\frac{|\boldsymbol{r}|^2}{4Dvt} - \mu_a vt\right) \tag{1.12}$$

Boundary conditions

The boundary condition in the infinite case simply consists in imposing that the fluence go to zero at infinite distance. In a more general case, for finite geometries, we must impose that the radiation entering the diffusive medium at the boundary originates from the Fresnel reflection of the outgoing radiation. Within the Diffusion Approximation, this boundary condition assumes the form [2]:

$$\Phi(\boldsymbol{r}, t) = z_b \hat{\boldsymbol{n}} \cdot \boldsymbol{\nabla} \Phi(\boldsymbol{r}, t) \qquad \text{on the interface} \tag{1.13}$$

Here $\hat{\boldsymbol{n}}$ is the outgoing unit vector normal to the surface, and z_b is given by:

$$z_b = 2D \frac{1 - R_{\text{eff}}}{1 + R_{\text{eff}}} = \frac{2}{3\mu_s'} \frac{1 - R_{\text{eff}}}{1 + R_{\text{eff}}} \tag{1.14}$$

where R_{eff} is the effective Fresnel coefficient at the interface, which can be approximated as a series development of the relative refractive index $n = n_{\text{medium}}/n_{\text{out}}$: $R_{\text{eff}} \simeq -1.440n^{-2} + 0.710n^{-1} + 0.668 + 0.00636n$.

Equation (1.13), also known as *partial-current boundary condition,* is relatively difficult to apply in practice, so it is usually forgone in favour of the so-called *extrapolated-zero boundary condition.* This is obtained by assuming that the derivative of the fluence along the normal direction outside the medium is constant and equal to its value on the boundary. Doing this, we get that the fluence reaches zero at a distance z_b from the interface outside the medium:

$$\Phi(z = -z_b) = 0 \tag{1.15}$$

which is much easier to implement, while still approximating the exact condition quite well [20].

Solution for the semi-infinite medium

The solution for the infinite medium is useful to describe situations where the boundaries of the diffusive medium are far from the source with respect to the effective attenuation length $\ell_{\text{eff}} = 1/\sqrt{3\mu_a\mu_s'}$. In many applications we are interested instead in studying the propagation of light through a medium with well-defined boundaries, detecting the radiation exiting from the medium. Let's suppose we are shining a collimated beam of light perpendicular to the surface of a diffusive medium. In order to model such a source with isotropic ones, we would need a line of point-like sources with decreasing intensity described by Lambert's law in which both absorption and scattering are present:

$I(z) = I(0)e^{-(\mu_a+\mu'_s)z}$ where z is the depth coordinate. However, for the sake of simplicity the source is typically modelled as one isotropic source placed at a depth $z_0 = \ell'$ [2]. This approximation is justified by the fact that the center of mass of Lambert's distribution is $z_1 = (\mu_a + \mu'_s)^{-1} \simeq (\mu'_s)^{-1} = z_0$.

Applying the extrapolated-zero boundary condition in this situation can be conveniently done making use of the method of images, that is, introducing a negative source at $z_s = -2z_b - z_0$ with the same intensity as the positive one. The fluence can then be calculated as the solution for the infinite medium with these two sources, which is the sum of the two solutions. Using a cylindrical coordinate system, where z is the depth and r the radial coordinate, we get:

$$\Phi(r, z, t) = \frac{vQ_0}{(4\pi Dvt)^{3/2}} e^{-\mu_a vt} \left[\exp\left(-\frac{r^2 + (z - z_0)^2}{4Dvt} \right) - \exp\left(-\frac{r^2 + (z - z_s)^2}{4Dvt} \right) \right] \quad (1.16)$$

However, in practical applications we are not interested in the fluence, but rather in the *reflectance* R, defined as follows: $R(r, t)$ is the power per unit area leaving the medium at time t and distance r from the injection point on the medium surface, irrespective of exit direction. The reflectance can be obtained by the flux vector, as the component of the flux in the direction orthogonal to the surface. Using Fick's law we can write:

$$R(r, t) = |J_z(r, z = 0, t)| = \left| -D \frac{\partial \Phi(r, z, t)}{\partial z} \right|_{z=0}$$

Substituting eq. (1.16), we get:

$$R(r, t) = \frac{Q_0}{2t^{5/2}(4\pi Dv)^{3/2}} \exp\left(-\frac{r^2}{4Dvt} - \mu_a vt \right) \left[z_0 \exp\left(-\frac{z_0^2}{4Dvt} \right) - z_s \exp\left(-\frac{z_s^2}{4Dvt} \right) \right] \quad (1.17)$$

The reflectance is plotted as a function of time and for different values of μ_a, μ'_s, r in fig. 1.1. Notice that the absorption coefficient mainly influences the tail of the time distribution of photons (fig. 1.1a): the lower the absorption, the later the last photons can arrive at the detector before being absorbed. Scattering, on the other hand, influences the time of detection of the earliest photons (fig. 1.1b): the lower the scattering, the sooner the first photons are detected. Finally, the source-detector separation r determines the position of the peak as well as the intensity of the signal (fig. 1.1c).

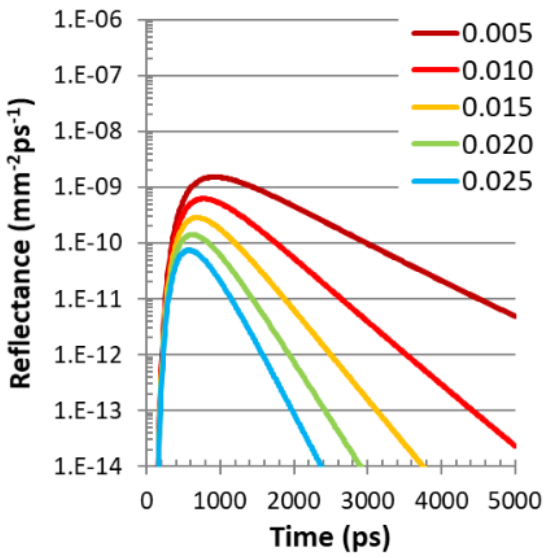

(a) μ_a variable (units in the legend are mm^{-1}), $\mu_s' = 1\,\mathrm{mm}^{-1}$, $r = 30\,\mathrm{mm}$

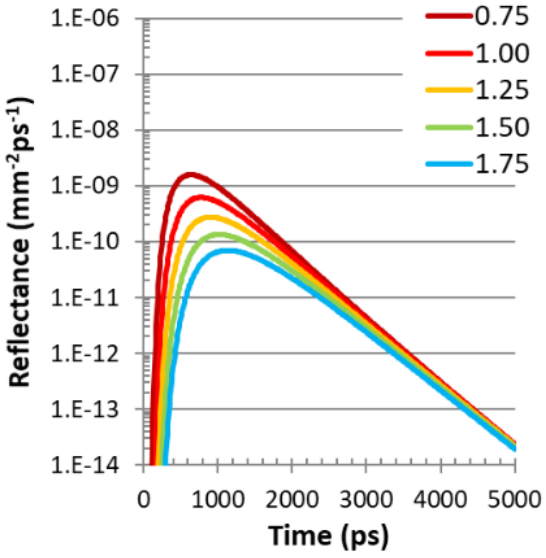

(b) $\mu_a = 0.01\,\mathrm{mm}^{-1}$, μ_s' variable (units in the legend are mm^{-1}), $r = 30\,\mathrm{mm}$

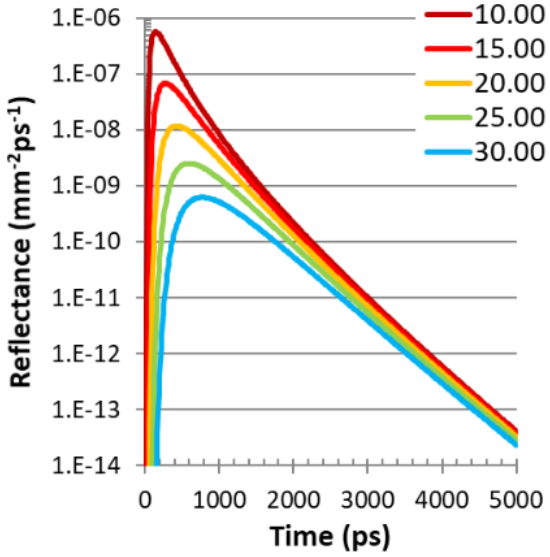

(c) $\mu_a = 0.01\,\mathrm{mm}^{-1}$, $\mu_s' = 1\,\mathrm{mm}^{-1}$, r variable (units in the legend are mm)

Figure 1.1: Plots of the reflectance (normalized to the source amplitude Q_0) in a semi-infinite medium as a function of time for different values of μ_a, μ_s' and r. Note the logarithmic scale on the vertical axis.

1.3. Diffuse Correlation Spectroscopy

In this section the physical basis of DCS will be presented. In a typical DCS experiment, light is shone inside a tissue and then the emerging scattered radiation is detected, similar to TRS. However, in DCS the quantity of interest is the temporal autocorrelation of photons, rather than their density, since it contains information on the motion of scatterers inside the medium.

1.3.1. Quantities used to describe scattering by fluctuations

When studying light-matter interaction we often assume that media are homogeneous, however this is only true from a statistical point of view. For example, while the average number of molecules is a certain volume can be assumed constant, their instantaneous number varies. Such statistical fluctuations in concentration, density or orientation of molecules give rise to a type of scattering different from the one that has been considered so far.

The quantities used to describe this phenomenon are the first- and second-order autocorrelation functions. The *first-order autocorrelation function* $G_1(t_1, t_2)$, also called *field autocorrelation function*, is defined as:

$$G_1(t_1, t_2) = \langle \boldsymbol{E}^*(t_1) \cdot \boldsymbol{E}(t_2) \rangle$$

where $\boldsymbol{E}(t)$ is the detected electric field at time t, the * symbol denotes the complex conjugate and the angled brackets have the usual meaning of ensemble average. In the following we shall assume ergodic processes, so that the ensemble average can be substituted with the temporal average. Moreover, since ergodic processes are stationary, the value of $G_1(t_1, t_2)$ only depends on the time difference $\tau = t_2 - t_1$ rather than the absolute time instants. We can therefore define G_1 as:

$$G_1(\tau) = \langle \boldsymbol{E}^*(t) \cdot \boldsymbol{E}(t + \tau) \rangle$$

A normalized version of the first-order autocorrelation is also used:

$$g_1(\tau) = \frac{G_1(\tau)}{\langle \boldsymbol{E}^*(t) \cdot \boldsymbol{E}(t) \rangle} = \frac{\langle \boldsymbol{E}^*(t) \cdot \boldsymbol{E}(t + \tau) \rangle}{\langle \boldsymbol{E}^*(t) \cdot \boldsymbol{E}(t) \rangle}$$

for which $g_1(0) = 1$ holds.

In practical application the electric field is not measured, rather the intensity of the radiation is. For this reason we introduce the *second-order autocorrelation,* or *intensity autocorrelation,* as:

$$G_2(\tau) = \langle I(t)I(t+\tau)\rangle$$

where $I(t)$ is the detected intensity. Its normalized version is obtained by dividing by the square of the ensemble average of the intensity:

$$g_2(\tau) = \frac{G_2(\tau)}{\langle I(t)\rangle^2} = \frac{\langle I(t)I(t+\tau)\rangle}{\langle I(t)\rangle^2}$$

The following properties hold for $g_2(\tau)$:

1. g_2 is an even function: $g_2(-\tau) = g_2(\tau)$;
2. g_2 is a decreasing function: $g_2(\tau) \leq g_2(0)$.
3. $g_2 \to 1$ for $\tau \to \infty$.

The physical meaning of the second property is clear: for small values of the delay the particles have undergone small fluctuations, thus not influencing the intensity much. For bigger values of τ the intensity loses autocorrelation, eventually decaying to 1 for long delays. For perfectly coherent light (no fluctuations) $g_2(\tau) \equiv 1$, while the faster the intensity varies, the sooner the autocorrelation decays.

The normalized first- and second-order autocorrelation curves are tied by the so-called *Siegert relation,* which reads:

$$g_2(\tau) = 1 + \beta|g_1(\tau)|^2 \tag{1.18}$$

where $\beta \leq 1$ is a dimensionless parameter that depends on the experimental conditions (in particular on the coherence length of the light source, the wavelength, the source-detector separation and the aperture of the optical detection system), being equal to 1 for an ideal setup [2]. In a typical experiment its value cannot be determined *a priori,* and is instead retrieved by the measured value of g_2: $\beta = g_2(0) - 1$.

1.3.2. The Correlation Transport Equation and its Diffusion Approximation

The first-order correlation function for light propagating through a turbid medium can be obtained as the solution of the so-called *Correlation Diffusion Equation* (CTE), which

is analogous to the RTE [2]:

$$\begin{aligned}\frac{1}{v}\frac{\partial}{\partial t}G_1^T(\boldsymbol{r},\hat{\boldsymbol{s}},t,\tau) = &-\hat{\boldsymbol{s}}\cdot\boldsymbol{\nabla}\left[G_1^T(\boldsymbol{r},\hat{\boldsymbol{s}},t,\tau)\right] - (\mu_a+\mu_s)\,G_1^T(\boldsymbol{r},\hat{\boldsymbol{s}},t,\tau)\\ &+\mu_s\int_{4\pi} g_1^s(\hat{\boldsymbol{s}},\hat{\boldsymbol{s}}',\tau)\,p(\hat{\boldsymbol{s}},\hat{\boldsymbol{s}}')\,G_1^T(\boldsymbol{r},\hat{\boldsymbol{s}}',t,\tau)\,\mathrm{d}\Omega' + \varepsilon(\boldsymbol{r},\hat{\boldsymbol{s}},t)\end{aligned} \tag{1.19}$$

Here the function $g_1^s(\hat{\boldsymbol{s}},\hat{\boldsymbol{s}}',\tau)$ is the normalized first-order correlation obtained in single-scattering regime. $G_1^T(\boldsymbol{r},\hat{\boldsymbol{s}},t,\tau)$ represents the correlation function depending on the position $\boldsymbol{r}$, direction $\hat{\boldsymbol{s}}$ and time t, on top of the delay τ. The unnormalized correlation function $G_1(\boldsymbol{r},t,\tau)$ is obtained by integrating G_1^T over all possible directions:

$$G_1(\boldsymbol{r},t,\tau) = \int_{4\pi} G_1^T(\boldsymbol{r},\hat{\boldsymbol{s}},t,\tau)\,\mathrm{d}\Omega$$

With reference to the RTE (eq. (1.8) on page 9) then G_1^T is analogous to the radiance, while G_1 to the fluence.

Adopting the Diffusion Approximation it is possible to obtain a Diffusion Equation for the correlation function, which in stationary regime (CW sources) in a homogeneous medium assumes the form [7]:

$$\left[-D\nabla^2 + \left(\mu_a + \frac{\alpha}{3}k_0^2\mu_s'\left\langle\Delta r^2(\tau)\right\rangle\right)\right]G_1(\boldsymbol{r},\tau) = q_0(\boldsymbol{r}) \tag{1.20}$$

where:

- α is the ratio of moving scatterers to total scatterers. In liquid phantoms used for laboratory measurements $\alpha \simeq 1$, while in biological tissue it is generally unknown.
- $k_0 = 2\pi/\lambda$ is the wave number of light in the medium;
- $\langle\Delta r^2(\tau)\rangle$ is the mean-square displacement of moving scatterers in time τ. In many practical applications of DCS in living tissues the motion of scatterers (red blood cells) is well approximated by a Brownian model, that is $\langle\Delta r^2(\tau)\rangle = 6D_B\tau$, where D_B is the *effective diffusion coefficient* of the moving scatterers (larger by a few orders of magnitude than the value given by the Einstein relation) [2].

It is immediate to see that the Correlation Diffusion Equation (eq. (1.20)) is analogous to the Diffusion Equation for the fluence (eq. (1.10) on page 11), taking care of adding the term $\alpha k_0^2\mu_s'\langle\Delta r^2(\tau)\rangle/3$ to the absorption coefficient. The solution for the semi-infinite

medium is then [21]:

$$G_1(r,\tau) = \frac{vQ_0}{4\pi D}\left\{\frac{\exp[-K(\tau)\, r_1]}{r_1} - \frac{\exp[-K(\tau)\, r_2]}{r_2}\right\} \tag{1.21}$$

where Q_0 is the amplitude of the delta-like source, $r_1 = \sqrt{r^2 + z_0^2}$, $r_2 = \sqrt{r^2 + z_s^2}$ and $K(\tau) = \sqrt{3\mu_a\mu_s' + \alpha k_0^2 \mu_s'^2 \langle \Delta r^2(\tau)\rangle}$.

The normalized solutions in the case of Brownian motion for both the field and intensity autocorrelation functions are plotted in fig. 1.2 for different values of D_B and r. Notice how higher values of D_B (fig. 1.2a) and r (fig. 1.2b) cause the scattered light to lose correlation sooner.

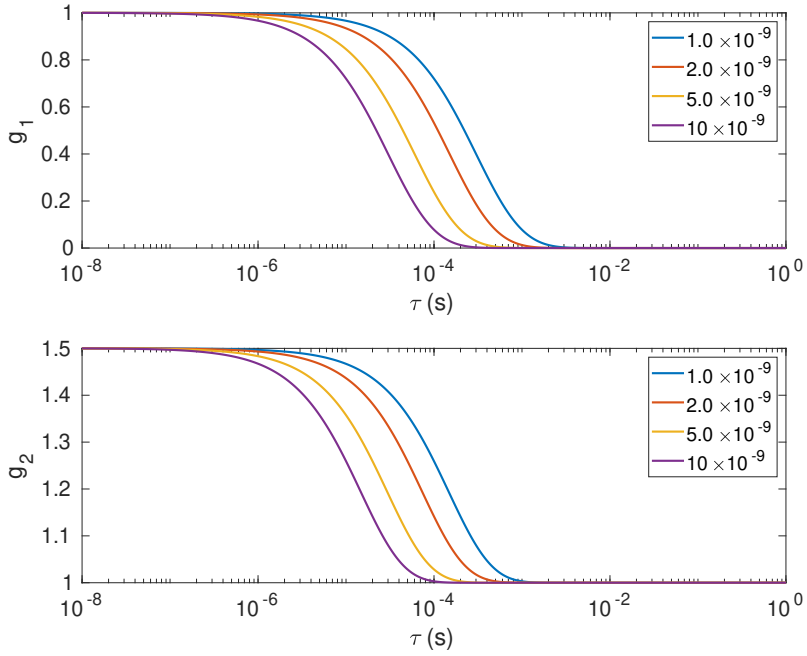

(a) D_B variable (units in the legend are $\mathrm{cm^2\,s^{-1}}$), $r = 2\,\mathrm{cm}$

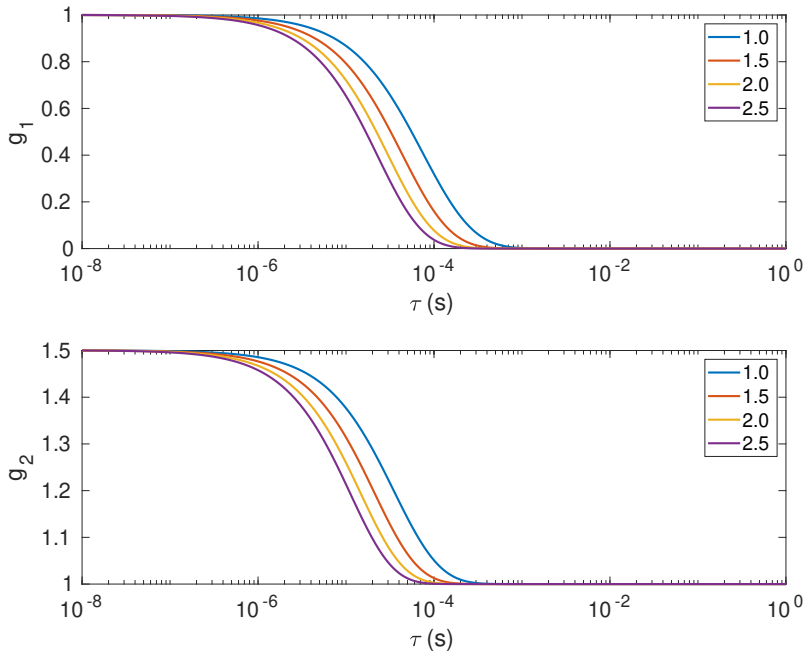

(b) $D_B = 1 \times 10^{-8}\,\mathrm{cm^2\,s^{-1}}$, r variable (units in the legend are cm)

Figure 1.2: Plots of the normalized first- and second-order correlation functions for light scattered by particles undergoing Brownian motion. Note the logarithmic scale on the horizontal axis. The value of the parameters are $\alpha = 1$, $\beta = 0.5$, $\lambda = 784\,\mathrm{nm}$, $\mu_a = 0.1\,\mathrm{cm^{-1}}$, $\mu_s' = 10\,\mathrm{cm^{-1}}$, $n = 1.44$.

2 | Materials and methods

"We are stuck with technology when what we really want is just stuff that works"
– Douglas Adams

In this chapter the experimental setups used for both TRS and DCS will be illustrated, along with explanations of the data collection modalities. Finally, a few different software autocorrelation algorithms will be described.

2.1. Experimental setup

The overall instrument is made of two separate setups: a TRS module and a DCS one. Time-domain Reflectance Spectroscopy allows to retrieve the tissue optical parameters μ_a and μ_s', which are then used in fitting the autocorrelation curve measured by the DCS setup to retrieve the blood flow index BFI $= \alpha D_B$. Note that in principle the DCS technique is able to retrieve all variables of interest by fitting eq. (1.21) with all of them at once, however doing this would yield inaccurate results. In particular, errors in the estimation of the optical parameters would cause further errors in the evaluation of the diffusion coefficient [21]. Moreover, the use of both DCS and TRS allows to measure quantities that the two techniques are not able to retrieve when only one of them is used, such as the cerebral metabolic rate of oxygen consumption ($CMRO_2$) [7, 10].

Both the TRS and DCS modules feature multiple detection channels that work in parallel, allowing to collect light from different points of the investigated sample. This way it is possible to perform measurements at different source-detector separations, which allows to separate the contributions of the superficial layers from those of deeper tissue. Indeed, since the DCS setup operates in continuous wave (CW), the penetration depth of the photons depends on the source-detector distance: the further apart injection and detection are, the deeper the detected photons have probed the medium (if r is the inter-fiber distance, the mean penetration depth is $\simeq r/2$ [2]). This feature is not shared by time-domain techniques such as TRS, for which penetration depth is independent of source-detector separation [5]. Nevertheless, working simultaneously at two different inter-fiber

Figure 2.1: Picture of the NIRSBOX used in the setup

distances allows the implementation of more complex models than the homogeneous one, such as the bilayer geometry [22, 23].

As for the DCS module, a software correlator was chosen as opposed to a hardware one. Being designed to fulfill a single task, hardware correlators are fast and easy to use, but they lack flexibility (for example, they typically have a fixed lag-time scale). Software correlators on the other hand are more cost-effective and flexible: since they operate on the raw photon time-tag stream, it is possible to pre-process this signal before calculating the autocorrelation, for example removing the noise of the laser source. Moreover, storing the raw time tags holds the potential for post-processing, investigating other methods for extracting blood flow information [24].

2.1.1. TRS setup

Time-domain reflectance spectroscopy is performed thanks to a NIRSBOX (manufactured by PIONIRS s.r.l.) [25], the compact device represented in fig. 2.1. Actually, this instrument differs from its standard commercial counterparts in that it features two detection channels as opposed to a single one. The system employs two lasers at different wavelengths, which operate in a time-multiplexing scheme in order to avoid cross-talk. This feature allows to measure the concentrations of both oxy- and deoxy-hemoglobin: as shown in fig. 1 on page 2 the two have different absorption spectra, so by measuring the total absorption coefficient and inverting eq. (1.2) on page 6, it is possible to get both concentrations. Since two unknowns must be retrieved, at least two equations are needed, hence the need for two different wavelengths.

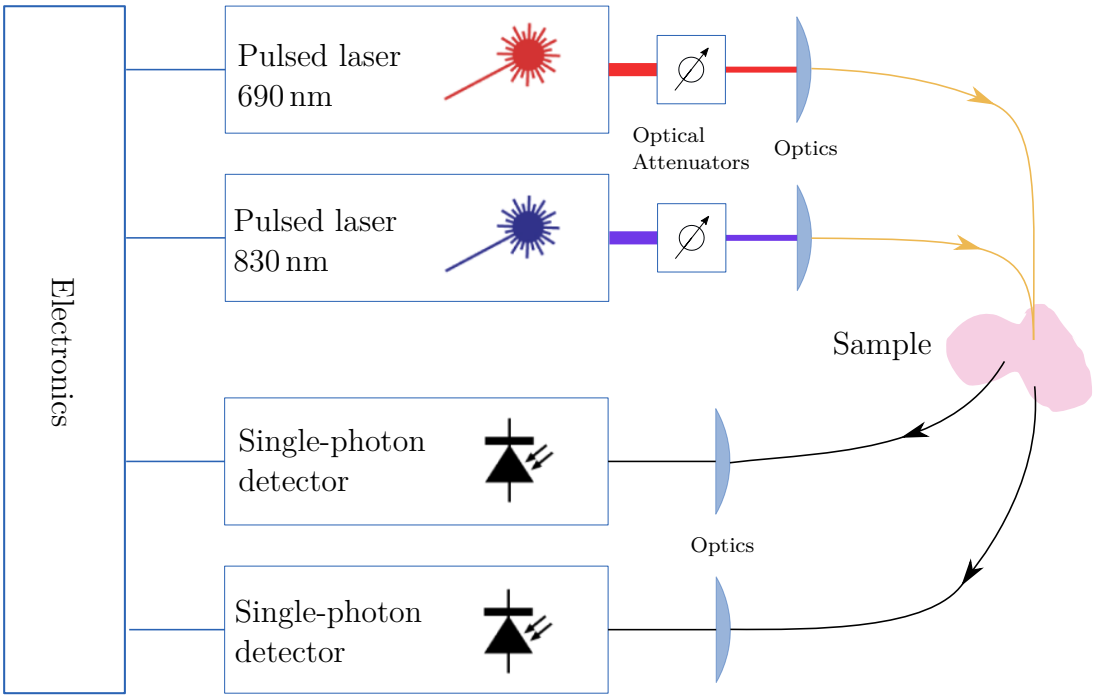

Figure 2.2: Simplified block scheme of the NIRSBOX (adapted from [25])

Figure 2.2 shows a block scheme of the NIRSBOX. The light sources are pulsed-diode lasers, operating in gain-switching mode at 50 MHz, emitting light at 690 nm (average output power 4 mW) and 830 nm (average output power 3.5 mW), respectively. The light produced by each source passes through an optical attenuator and is then coupled into a 100 µm graded-index glass optical fiber. In order to obtain a single injection point, the two input fibers are bundled together. The light scattered by the sample is collected by two graded-index plastic optical fibers with a core diameter of 0.9 mm and detected by two silicon photomultipliers with an active area of 1.3×1.3 mm^2. Time-to-digital conversion is performed by an application-specific integrated circuit (ASIC), allowing reconstruction of the distribution of photon time-of-flight (DTOF).

The instrument is connected to a computer, which controls the NIRSBOX through the homonym software. This allows to adjust the optical attenuators that regulate the output laser power, select the integration time for each iteration as well as visualize the DTOF curves and save the data in real-time. Even though the second detector effectively doubles the amount of data to be acquired compared to a standard NIRSBOX, the instrument is fast enough to calculate both histograms during an iteration before the next one starts.

In a TRS experiment the reflectance is measured as a function of time for a fixed source-detector separation. However, the resulting curve is not simply the one given by eq. (1.17) on page 13, but it also contains the response of the measurement setup. More precisely,

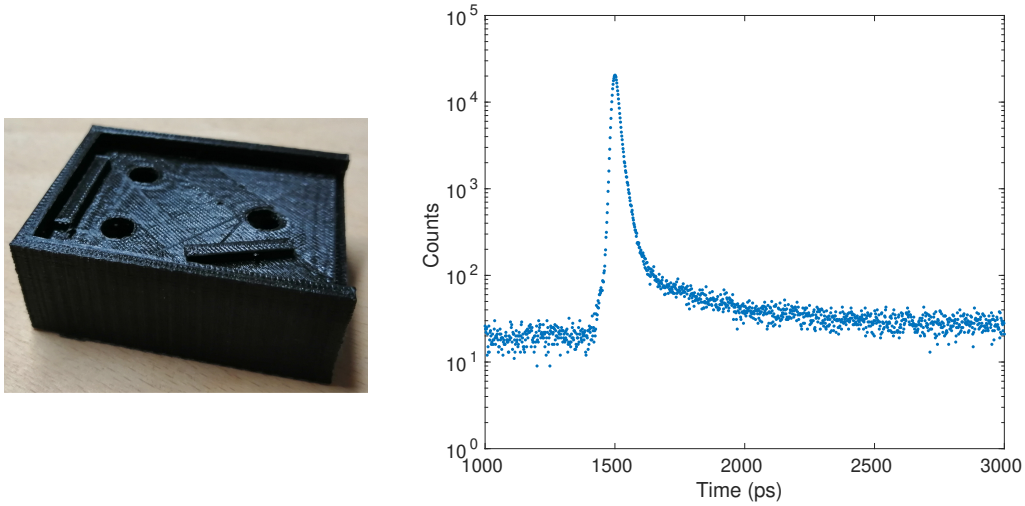

(a) IRF box (b) Plot of an IRF

Figure 2.3: Picture of the IRF box used in the setup and example of an IRF

the detected reflectance is:

$$R_{\text{meas}}(t) = [R_{\text{theor}} * \text{IRF}](t) = \int R_{\text{theor}}(t')\text{IRF}(t - t')\,\mathrm{d}t'$$

where $*$ denotes the convolution product and IRF represent the *instrument response function,* that is, the output measured by the device when no sample is present. In an ideal situation the IRF would be delta-shaped, and the measured curve would coincide with the theoretical one. Ideally, every time a measurement is performed the IRF is taken as well. By then convolving the theoretical solution with the measured IRF and fitting the resulting curve to the measured reflectance it is possible to retrieve the values of the tissue optical parameters (μ_a and μ_s').

In order to measure the IRF of the TRS setup, the custom box represented in fig. 2.3a was 3D-printed. The three holes on the top are positioned so as to align with the injection and detection fibers; the inside is coated in aluminium in order to better reflect the light. An example of IRF is plotted in fig. 2.3b.

2.1.2. DCS setup

The DCS module uses a single CW laser, four single-photon detectors and a time-tagging module connected to a PC that calculates the autocorrelation of the incoming photon stream. A block diagram of the setup is presented in fig. 2.4.

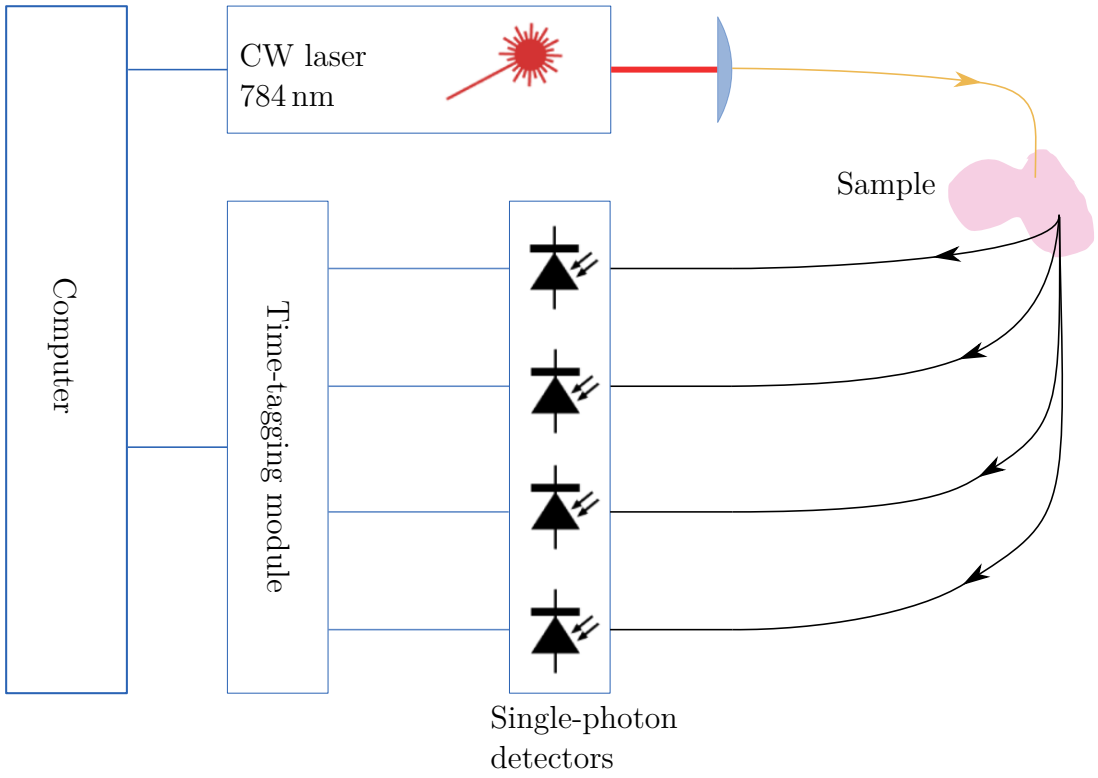

Figure 2.4: Simplified block scheme of the DCS module

The light source is a laser diode (iBeam smart WL by TOPTICA Photonics) emitting at 784 nm with high coherence length (> 8 m). This feature is critical to DCS, since the technique is based on measuring the interference of light diffused by the sample. The maximum reachable output power is 120 mW. The light emitted by the laser is coupled into a multi-mode glass/silica step-index fiber, whose core diameter is 400 µm. The diffused light is collected by four single-mode fibers (core diameter 4.4 µm), which ensure that the coherence of the diffused light is preserved. Four single-photon detectors (SPCM-AQRH by Excelitas Technologies) work in parallel to convert the light signal into an electric one. These are silicon avalanche photodiodes with 180 µm active area diameter, characterized by 250 ps temporal resolution and 20 ns dead time. Finally, the multi-channel time tagger (TimeTagger 20 by Swabian Instruments) allows digital data acquisition.

Differently from previously developed systems the DCS module does not make use of any hardware correlator, relying instead on the time-tagging module that reads the times of arrival of the incoming photons on the four channels. This raw data must then be analyzed by the computer. In order to achieve this the C# software shown in fig. 2.5 was developed, that on top of processing the data also controls the laser source, allowing to switch it on and off as well as adjust its output power. Once the measurement is started,

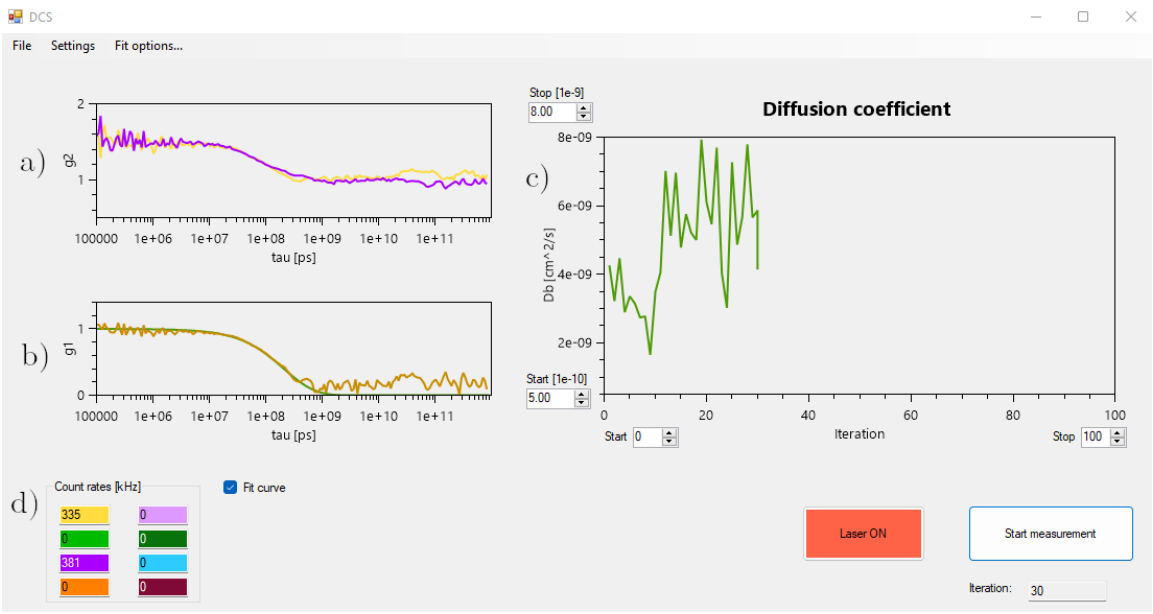

Figure 2.5: Screenshot of the main software window. a) Plots of the $g_2(\tau)$ functions (one curve per detector). b) Plot of the $g_1(\tau)$ function (brown) and the fitting curve (green). c) Plot of the temporal evolution of the diffusion coefficient $D_B(t)$. d) Count rates detected at each channel.

the time-tagger starts streaming the data to the software, which does the following:

- After the integration time has elapsed, four parallel threads calculate the second-order autocorrelation functions (one per detection channel) and plot them on-screen. The GUI also displays the count rates of each channel. Both the autocorrelations and the count rate are calculated using the APIs provided with the time-tagger.
- The four resulting g_2 curves are then averaged to obtain a single one, from which β is retrieved as $\beta = g_2(0) - 1$, where $g_2(0)$ is calculated as the average of the first few data points. The value of β is used to calculate $g_1(\tau)$, which is then fitted with the theoretical model (eq. (1.21) on page 18) to obtain the diffusion coefficient D_B. A second plot shows the measured $g_1(\tau)$ curve on top of the resulting fitting one. The fitting algorithm is provided by the ALGLIB library (`www.alglib.net`, Sergey Bochkanov).
- The value of D_B obtained from the fit is displayed on a third plot, which shows the time evolution of this parameter.
- Two data files in binary format are generated, the former containing the raw photon time-tags and the latter the autocorrelation curves and count rates. A third data file is updated, adding the new values of D_B and β.

- After another integration time has elapsed the process repeats, calculating, displaying, fitting and saving the new curves and displaying and saving the fit results.

The fitting and data saving operations are performed on a dedicated thread, which runs in parallel to the main data acquisition one. This ensures that no time tags are lost during data analysis.

The software allows the selection of a number of measurement parameters, including the integration time, how many and which detection channels to use, the refractive index of the medium, the inter-fiber distance and the fit parameters.

2.2. Software autocorrelation

As explained in section 2.1.2, the real-time software autocorrelation is calculated by the time-tagger API. However, several additional algorithms have been explored in post-processing in order to compare their performance, as detailed in section 3.2. These algorithms are illustrated in the following pages.

In a DCS experiment the intensity autocorrelation function is calculated by measuring the correlation of the electric pulses that come from the detector. Making use of the photon count rate $n(t)$ (as opposed to the intensity that has been considered in section 1.3.1), the normalized autocorrelation function can be written as:

$$g_n(\tau) = \frac{\langle n(t)\, n(t+\tau)\rangle}{\langle n(t)\rangle^2} \tag{2.1}$$

This equation is based on the assumption that the time resolution of the detection system is infinite, which is not safe to make in real experiments. In practice, the photon stream is always integrated over a finite time Δt, so that in place of $n(t)$ what is measured is actually the average count rate $\mu(t)$:

$$\mu(t) = \frac{1}{\Delta t}\int_{t-\Delta t/2}^{t+\Delta t/2} n(t')\,\mathrm{d}t' = n(t) * \frac{\Pi(t/\Delta t)}{\Delta t}$$

where $\Pi(x)$ represents the rectangle function, that is equal to 1 for $|x| < 0.5$ and 0 elsewhere. Thus the measured correlation function g_μ depends on the resolution Δt, being equal to [26]:

$$g_\mu(\tau) = g_n(\tau) * \frac{\Lambda(\tau/\Delta t)}{\Delta t} \tag{2.2}$$

where $\Lambda(x)$ is the triangular function, equal to $1 - |x|$ for $|x| < 1$ and 0 elsewhere. Equation (2.2) shows that the measured autocorrelation is a smoothed version of the

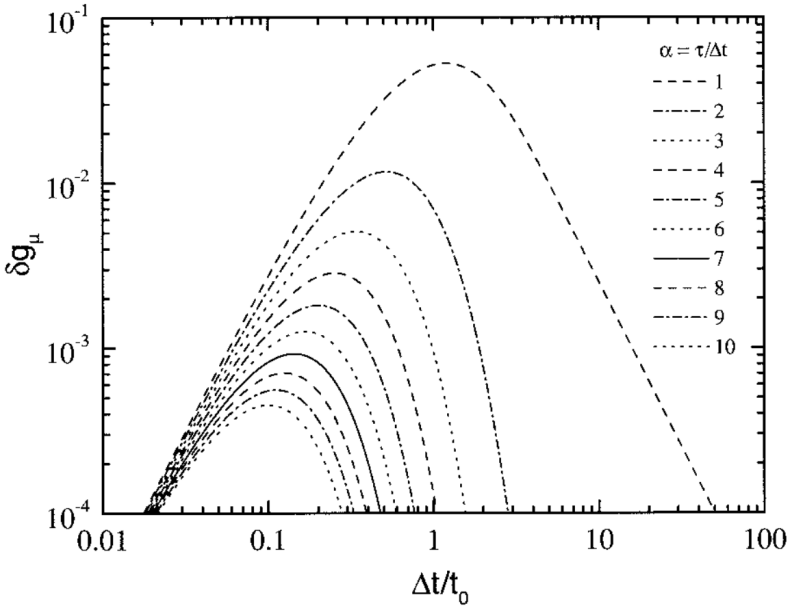

Figure 2.6: Error introduced by the finite resolution of the detection electronics for a single exponential decay, plotted as a function of the ratio between the sampling time Δt and the decay time t_0 of a single-exponentially decaying autocorrelation function. The various curves represent different values of $\alpha = \tau/\Delta t$. The plots refer to the case $A = 1$. From [26].

actual one, being a good approximation when g_n does not vary significantly over time scales of the order of Δt. Of course, in the limit $\Delta t \to 0$ (infinite temporal resolution) the triangular function tends to a Dirac delta and $g_\mu \to g_n$.

It can be shown that the error introduced by the triangular average in the case of a single exponential decay $g_n(\tau) = 1 + A\exp(-2\tau/t_0)$ is (for $\tau \gg \Delta t$) [26]:

$$\delta g_\mu(\tau) = g_\mu(\tau) - g_n(\tau) = Ae^{-2\tau/t_0}\left\{\left[\frac{\sinh(\Delta t/t_0)}{\Delta t/t_0}\right]^2 - 1\right\}$$

A plot of this error is shown in fig. 2.6 for different values of the ratio α between time delay τ and resolution Δt. It can be seen that the error is always positive, the maximum of the function is always in the range $\Delta t/t_0 \sim 0.1 \div 1$, and for large and small values of $\Delta t/t_0$ the error decays to zero. As expected, the greater α is, the lower the systematic error, in particular δg_μ is always lower than 10^{-3} when $\alpha > 7$. Such a small error can be easily masked by shot noise if measuring time or count rate are not too high. Finally, the reported case constitutes a "worst-case scenario", since it can be shown that for multi-exponential decays the error will always be bounded by the one calculated here [26].

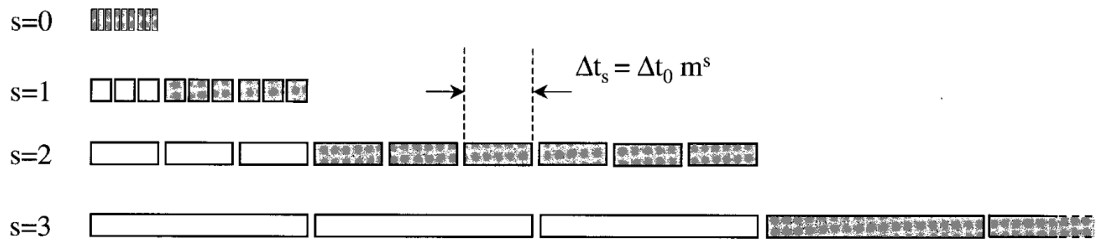

Figure 2.7: Schematic representation of the multi-tau scheme in the case $P = 9$, $m = 3$. Only the first four linear correlators are represented. The rectangles represent the bin size of each correlator, and the white ones are those that overlap with the previous correlator and are therefore discarded.

Multi-tau algorithms are based on a simple consideration: as long as the lag time τ is much greater than the sampling time Δt (α is high), there is no point in sampling the signal over time scales that are smaller than τ by orders of magnitude. Thus, before computing the autocorrelation function at time τ the signal is averaged over an integration time Δt chosen so as to keep α higher than a selected value. This way it is possible to reach high levels of accuracy while keeping computational efforts low, especially for big values of τ.

2.2.1. Classic multi-tau autocorrelation algorithm

This algorithm is based on a set of S linear correlators, with an integration time Δt_s that increases exponentially:

$$\Delta t_s = m^s \Delta t_0 \qquad s = 0, 1, \ldots, S-1$$

where Δt_0 is the binning rate of the counter and m the binning ratio. This way, if the first linear correlator is fed N_0 data points, the s-th correlator handles $m^{-s}N_0$ points. Each correlator computes the autocorrelation function of the input stream, averaged over Δt_s on a set of equally spaced lag times:

$$\tau_s(p) = p\Delta t_s \qquad s = 0, 1, \ldots, S-1$$

with $p = 0, 1, \ldots, P-1$, where P is the size of an array called *shift register* that is equal for all the correlators. This way, the first P/m bins of the s-th correlator overlap with all the bins of the $(s-1)$-th one, and are therefore discarded as shown in fig. 2.7. The lowest lag time for each correlator is $\tau_{s,\,\mathrm{min}} = (P/m)\Delta t_s$, therefore the corresponding minimum value of α is $\alpha_{\mathrm{min}} = P/m$ and the actual values of P and m can be chosen as needed. In most hardware correlators $P = 16$ and $m = 2$.

Each linear correlator uses the following algorithm for computing the autocorrelation. First, the shift register is loaded with the first P points. Then, the data stream is processed as follows. The latest datum is used to update the shift register: all of its components are moved to the right, the last one is discarded and the first one is replaced with the latest datum. Finally, all the components are multiplied by the latest datum, and the results are summed up in the autocorrelation array. Each multiplication corresponds to a different lag time on the same set of linear correlators.

2.2.2. Asynchronous autocorrelation algorithm

This algorithm, described in [27], works directly on the arrival times of the photons, without converting them into time-binned data beforehand. First, an integer B is chosen, from which a set of logarithmically spaced lag times is created:

$$\tau_j = \begin{cases} 1 & \text{if } j = 1 \\ \tau_{j-1} + 2^{\lfloor (j-1)/B \rfloor} & \text{if } j > 1 \end{cases}$$

where $\lfloor x \rfloor$ denotes the integer part of x. The result is a set of $j_{\max} = PB$ values of τ aggregated in P groups of B elements each with equal spacing of $2^{\lfloor j/B \rfloor}$.

The asynchronous algorithm then works as follows. For a given lag time $\bar{\tau}$, a vector of shifted arrival times $\{t'_k\}$ is calculated starting from the arrival times $\{t_k\}$ as $\{t'_k\} = \{t_k\} + \bar{\tau}$, and the value of the correlation for $\tau = \bar{\tau}$ is set to 0. Then the first array is scanned starting from the first element until the first t_j is found such that $t_j \geq t'_1$. If $t_j = t'_1$ then the autocorrelation for $\tau = \bar{\tau}$ is incremented by one. At this point, the algorithm switches to operating on the second vector, and starts scanning for the first value t'_{j_1} that is greater than or equal to t_{j_1}. If $t'_{j_1} = t_{j_1}$ then the value of the autocorrelation for $\tau = \bar{\tau}$ is again increased by one. The algorithm then switches back to the first vector and iterates the procedure until the last entries of both vectors are reached. This way, the obtained quantity is proportional to the probability that a photon was detected at time $t+\tau$, given that another one was detected at t.

This version of the algorithm however loses any information on periodic signals with a repetition time not included in the vector of lag times τ. To circumvent this, an averaging procedure is applied to coarsen the time resolution, that works as follows. In addition to the vectors $\{t_k\}$ and $\{t'_k\}$, all times are associated to weights $\{w_k\}$ and $\{w'_k\}$ which are all initially set to 1. When an equality $t_j = t'_\ell$ is found, the autocorrelation is incremented by the product $w_j w'_\ell$. Then, after a cascade of B lag times has been processed, all values $\{t_k\}$ used in the previous cascade are divided by 2 and rounded to the nearest lower integer.

This can lead to repeated consecutive entries, which are condensed into a single one, whose weight is increased by the sum of the weights of the eliminated entries. Finally, in order to correct for the varying time scale, at each lag time τ_j the calculated autocorrelation must be divided by $2^{\lfloor j/B \rfloor}$.

2.2.3. FFT-based autocorrelation algorithm

Finally, a simpler algorithm harnesses the efficiency of the well-known Fast Fourier Transform (FFT) [24]. The unnormalized second-order autocorrelation function $G_2(\tau) = \langle I(t)I(t+\tau)\rangle$ is similar to a convolution product of the intensity with itself, with the difference that in the latter case the intensity is not only shifted, but also flipped. Therefore, the autocorrelation function can be obtained as the convolution of $I(t)$ with $I(-t)$:

$$G_2(\tau) = [I(t) * I(-t)](\tau)$$

Thanks to the convolution theorem, the convolution product can be reduced to a simple algebraic one by moving to the frequency domain:

$$G_2(\tau) = \mathscr{F}^{-1}\{\mathscr{F}\{I(t)\}\mathscr{F}\{I(-t)\}\} = \mathscr{F}^{-1}\{\tilde{I}(\nu)\tilde{I}^*(\nu)\} = \mathscr{F}^{-1}\{|\tilde{I}(\nu)|^2\}$$

where $\mathscr{F}\{\cdot\}$ indicates the Fourier transform and $\tilde{I}(\nu) = \mathscr{F}\{I(t)\}$. Note that this result is the Wiener-Khinchin theorem, according to which an autocorrelation in the temporal domain corresponds to a square modulus operation in the frequency one.

Since the Fourier transform can be implemented efficiently by the FFT algorithm, the autocorrelation can be obtained in a very fast and stable manner. Note however that this algorithm is not a multi-tau one, since the FFT uses linearly spaced bins as opposed to logarithmically spaced ones.

3 | Phantom measurements

"I don't want to believe. I want to know"
– Carl Sagan

In order to assess the performance of both the TRS and DCS modules, a number of measurements were carried out on phantoms. These experiments are described in the present chapter, along with the results obtained.

3.1. Time-domain reflectance measurements

The NIRSBOX was characterized in terms of stability, linearity and accuracy. For the stability measurement the DTOF photon counts, barycenter position and full width at half-maximum (FWHM), as well as the retrieved optical parameters were measured for a long time. The goal was to reveal possible short- or long-term drifts of the measurands in time as well as fluctuations, which would be undesirable for clinical applications such as long-time monitoring.

To assess linearity and accuracy, the measured μ_a and μ_s' were compared with the ones yielded by a previously built instrument (a multi-wavelength TRS system used in the PHOOD laboratory [28]). Accuracy is critical for absolute measurements, to ensure that the instrument can retrieve physiological information correctly (such as oxy- and deoxy-hemoglobin concentration in tissue). Linearity is instead crucial for relative measurements, that is to be able to follow variations of such parameters in time without distortion.

The stability, linearity and accuracy of the TRS module were assessed through a set of measurements employing 32 solid phantoms, as prescribed by the MEDPHOT protocol [29]. These are epoxy resin phantoms labelled by a letter (A to D) and a number (1-8), referring to their scattering and absorption, respectively. In particular, the reduced scattering coefficients at 800 nm range from $\simeq 5\,\mathrm{cm}^{-1}$ for the A series to $\simeq 20\,\mathrm{cm}^{-1}$ for the D series, in steps of $5\,\mathrm{cm}^{-1}$; the absorption coefficients at the same wavelength range from $\simeq 0$ to $\simeq 0.49\,\mathrm{cm}^{-1}$ in steps of $0.07\,\mathrm{cm}^{-1}$.

3.1.1. Stability measurement

The B3 phantom was chosen for the stability measurement, due to its optical parameters resembling those of human tissue ($\mu_s' \simeq 10\,\mathrm{cm}^{-1}$, $\mu_a \simeq 0.14\,\mathrm{cm}^{-1}$). The inter-fiber distance was set to 3 cm for both detection channels, whose fibers were placed 2 cm apart. The optical attenuators were adjusted so as to detect about 10^6 photons on channel 1 for every reflectance curve. The measurement lasted about 4 hours, with integration time 1 s and detectors operating in parallel.

The time evolution during the measurement of the photon counts, full width at half-maximum (FWHM) and barycenter position of the curves is shown in figs. 3.1 to 3.3, while the time trace of the optical parameters is plotted in figs. 3.4 and 3.5 for both detectors and wavelengths. With the exception of the FWHM (fig. 3.3), whose average value is constant over the whole measurement, after an initial transitory of about 30 minutes (1000 repetitions) the instrument reaches stability, and the measured quantities are stationary. In all cases the oscillations stay within 3% of the mean value for the whole duration.

The values of the optical parameters retrieved by the two channels show small discrepancies (less than 2%) at 690 nm (fig. 3.4). This could be caused by inhomogeneities of the phantom, as well as thermal differences between the detectors; indeed detector 1 is placed inside the NIRSBOX, while detector 2 sits outside on top of the instrument (fig. 2.1 on page 22).

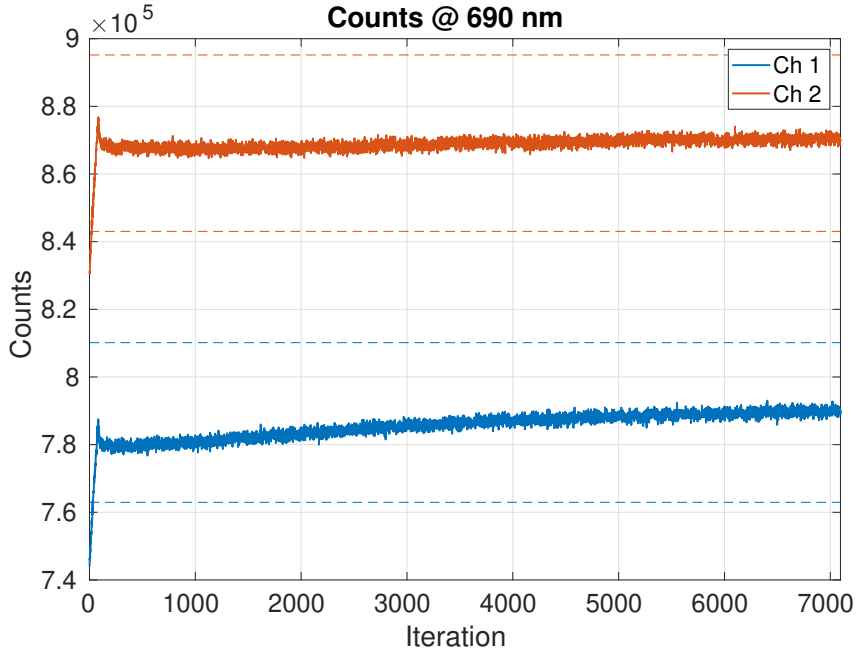

(a) Counts at $\lambda = 690\,\text{nm}$

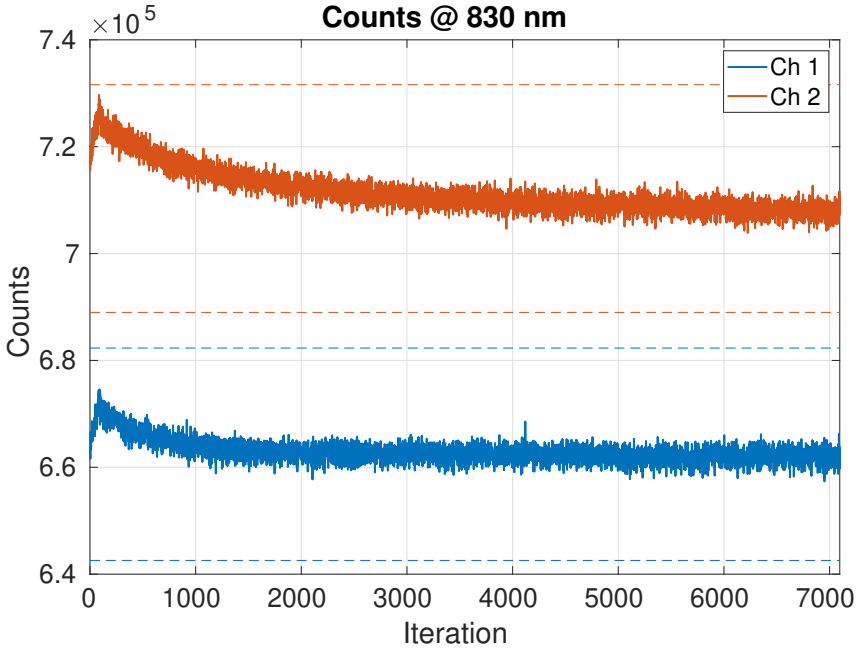

(b) Counts at $\lambda = 830\,\text{nm}$

Figure 3.1: Time evolution of the number of photons making up each curve during the stability measurement for both detection channels. The dashed lines are placed at ±3% of the respective values at regime.

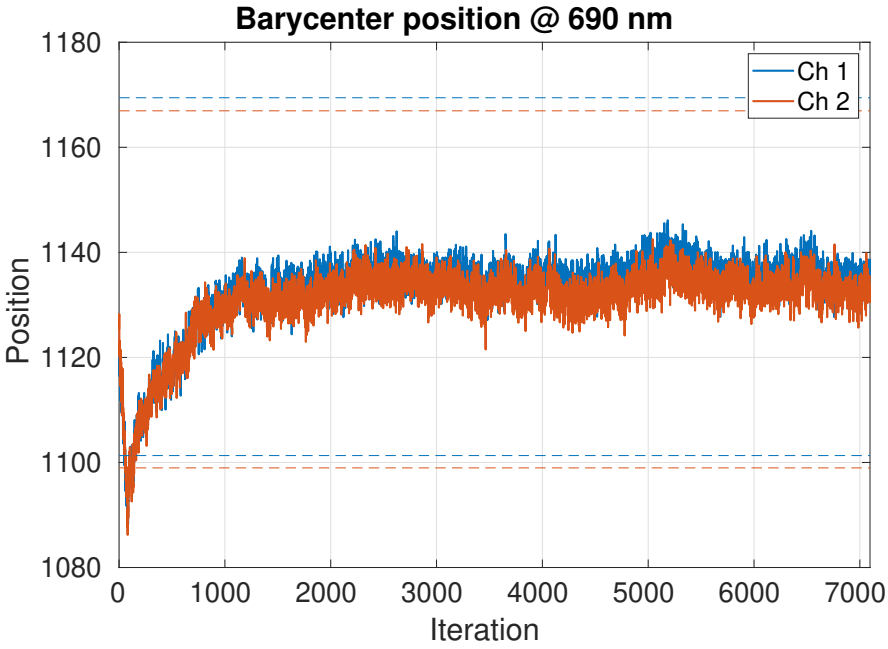

(a) Barycenter positon at $\lambda = 690\,\mathrm{nm}$

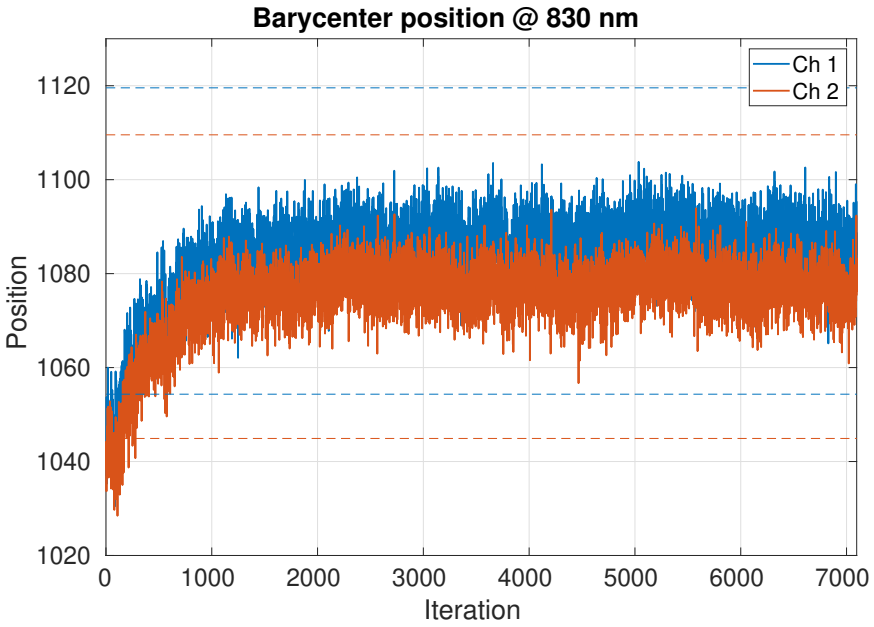

(b) Barycenter position at $\lambda = 830\,\mathrm{nm}$

Figure 3.2: Time evolution of the position of the barycenter of the photon time-of-flight distribution during the stability measurement for both detection channels. The dashed lines are placed at $\pm 3\%$ of the respective values at regime.

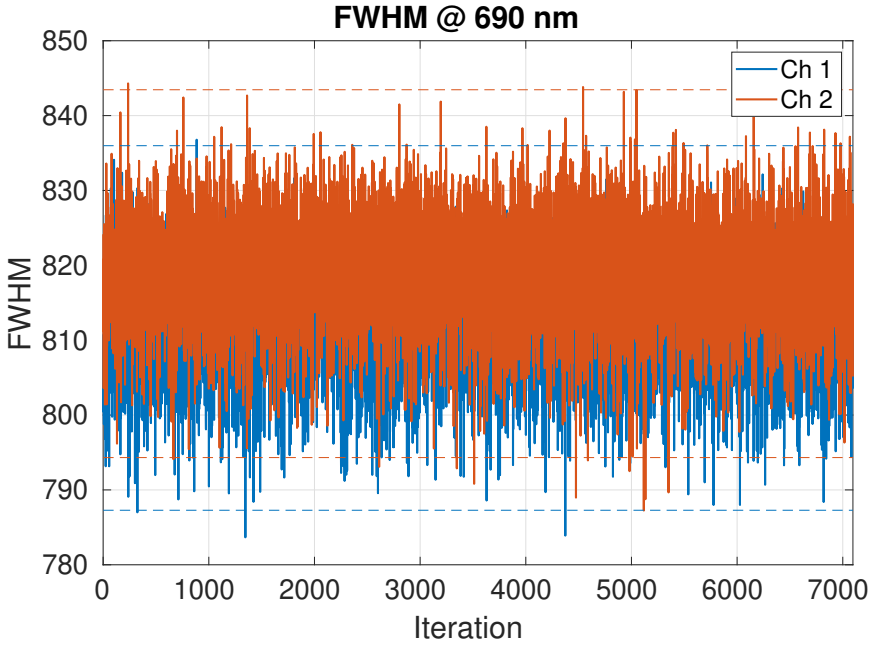

(a) FWHM at $\lambda = 690\,\mathrm{nm}$

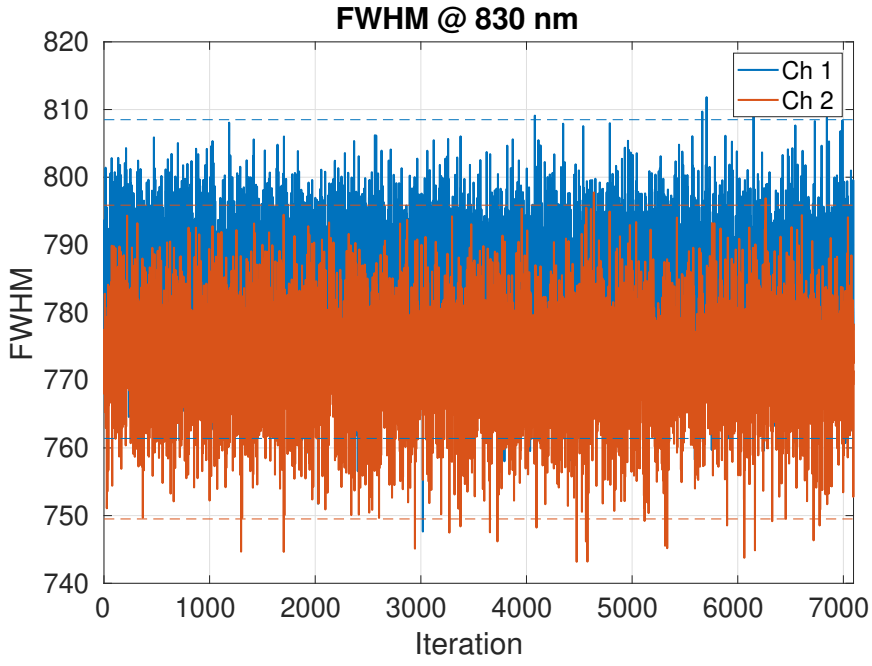

(b) FWHM at $\lambda = 830\,\mathrm{nm}$

Figure 3.3: Time evolution of the FWHM of the photon time-of-flight distribution during the stability measurement for both detection channels. The dashed lines are placed at $\pm 3\%$ of the respective values at regime.

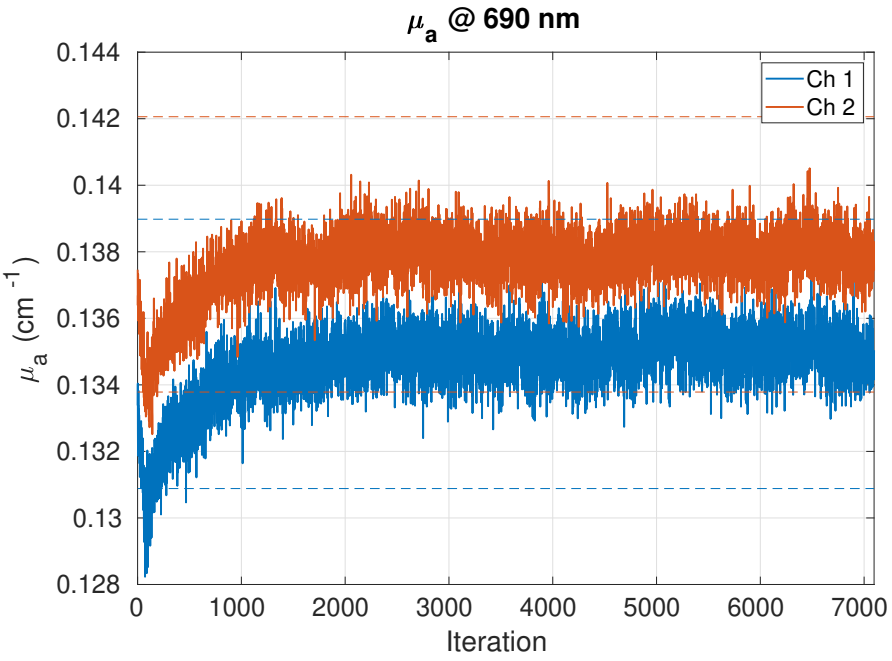

(a) Time evolution of μ_a

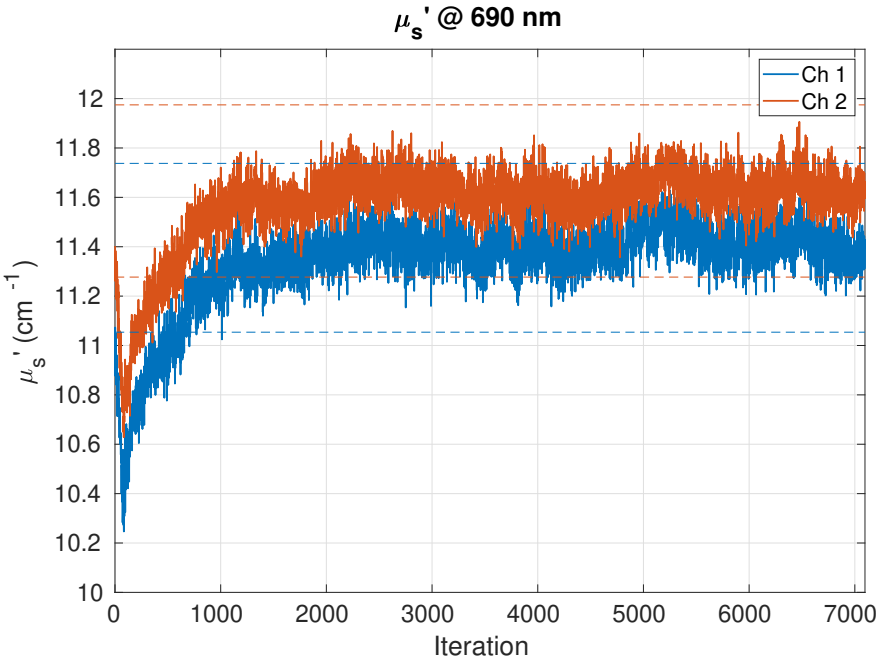

(b) Time evolution of μ_s'

Figure 3.4: Time evolution of the optical parameters at $\lambda = 690\,\text{nm}$ during the stability measurement for both detection channels. The dashed lines are placed at $\pm 3\%$ of the respective values at regime.

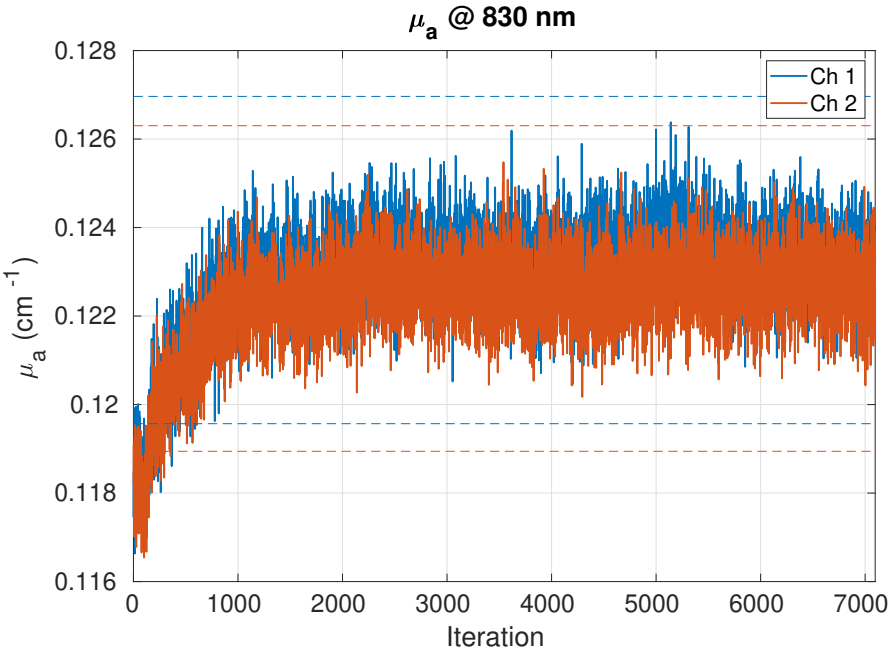

(a) Time evolution of μ_a

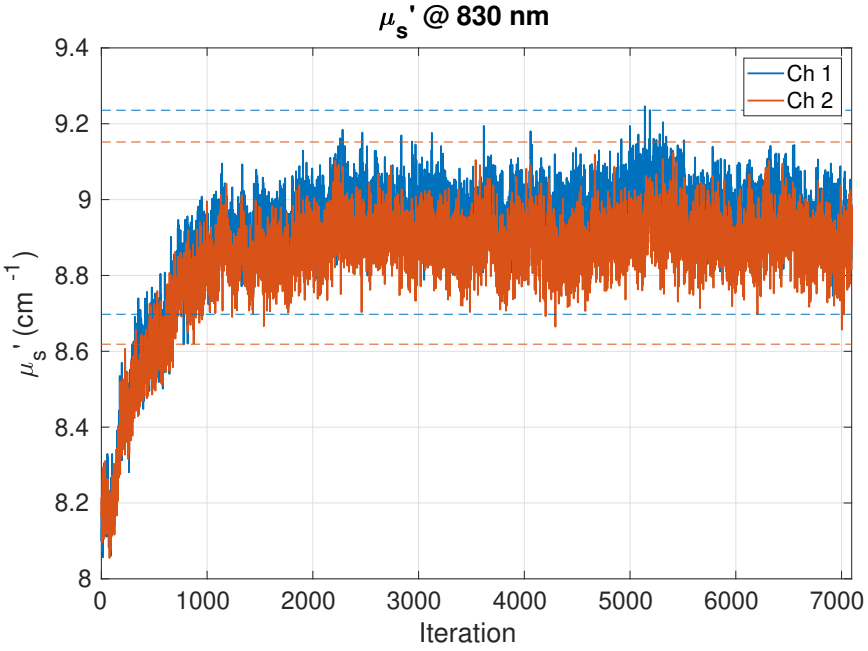

(b) Time evolution of μ_s'

Figure 3.5: Time evolution of the optical parameters at $\lambda = 830\,\text{nm}$ during the stability measurement for both detection channels. The dashed lines are placed at $\pm 3\%$ of the respective values at regime.

3.1.2. Linearity and accuracy measurements

To assess the linearity and accuracy of the instrument, a measurement on the full set of MEDPHOT phantoms was carried out. Each of the 32 phantoms was measured for 40 s with 1 s integration time so as to obtain 20 reflectance curves at each wavelength. Like the stability measurement, the optical attenuators were set so that detector 1 received about 10^6 photons per curve. The inter-fiber distance was 3 cm for both channels, whose detection fibers were placed 2 cm apart.

The values of μ_a are plotted in figs. 3.6 to 3.9 for the various scattering series, while the values of μ_s' are plotted in fig. 3.10. Both detection channels yield compatible values of the absorption and scattering coefficients across all phantoms. For highly absorbing ones (series 5-8) the values of μ_a measured are higher than the ones provided by the other instrument, but they show higher linearity. The phantoms with higher levels of absorption and scattering (C8, D6, D7, D8) give bigger error bars for both μ_a and μ_s'. This is due to the photons being absorbed or scattered away before reaching the detector, which results in lower signal-to-noise ratios: the peaks of the reflectance curves are higher than the background by one decade or less. This in turn causes less robust fitting of the resulting curves.

Figures 3.11 and 3.12 show the values of the optical parameters measured by the NIRSBOX compared to the "nominal" ones of the PHOOD instrument. In these plots each point represents an absorption (fig. 3.11) or scattering (fig. 3.12) series as measured by one detector, having as coordinates the average absorption (reduced scattering) coefficient across all phantoms of the same absorption (scattering) series. In particular, the horizontal coordinate is the average value yielded by the multi-wavelength instrument, while the vertical one is the one measured by the NIRSBOX. As already observed, the concordance on the values of μ_a is not perfect, while for μ_s' there is good agreement both at 690 nm and at 830 nm.

The relative errors on the estimation of the optical parameters are reported in table 3.1. The high relative errors of the absorption coefficients for series 1 are caused by the low absolute values of μ_a of these phantoms ($< 0.01\,\mathrm{cm}^{-1}$). Because of this, to obtain meaningful values, the average error calculated in table 3.1a refers to phantoms belonging to series 2-6, whose absorption coefficients mimic those of human tissue. For both optical parameters, at a given wavelength the two detection channels yield very similar average errors.

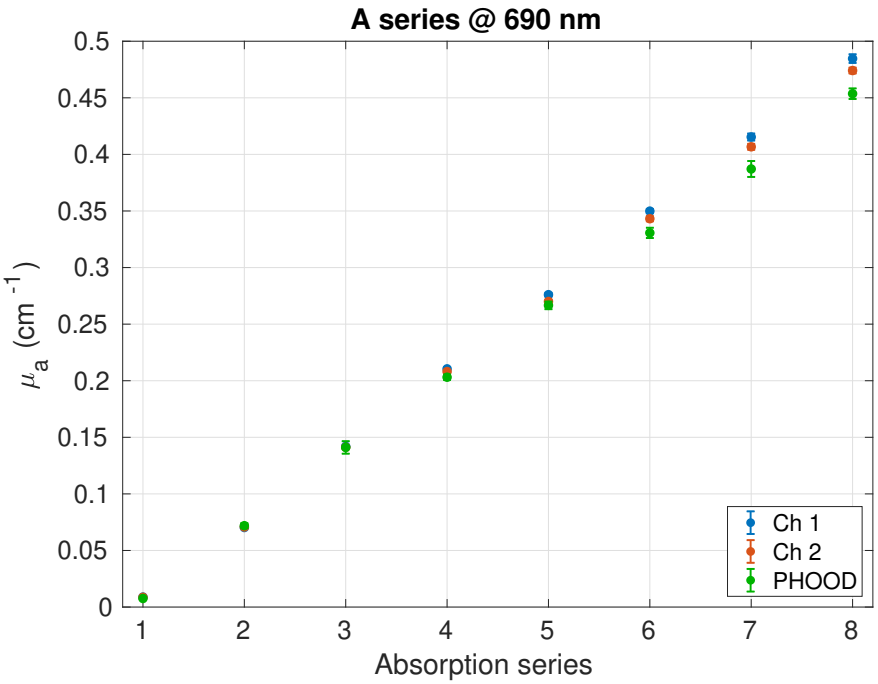

(a) μ_a at $\lambda = 690\,\mathrm{nm}$

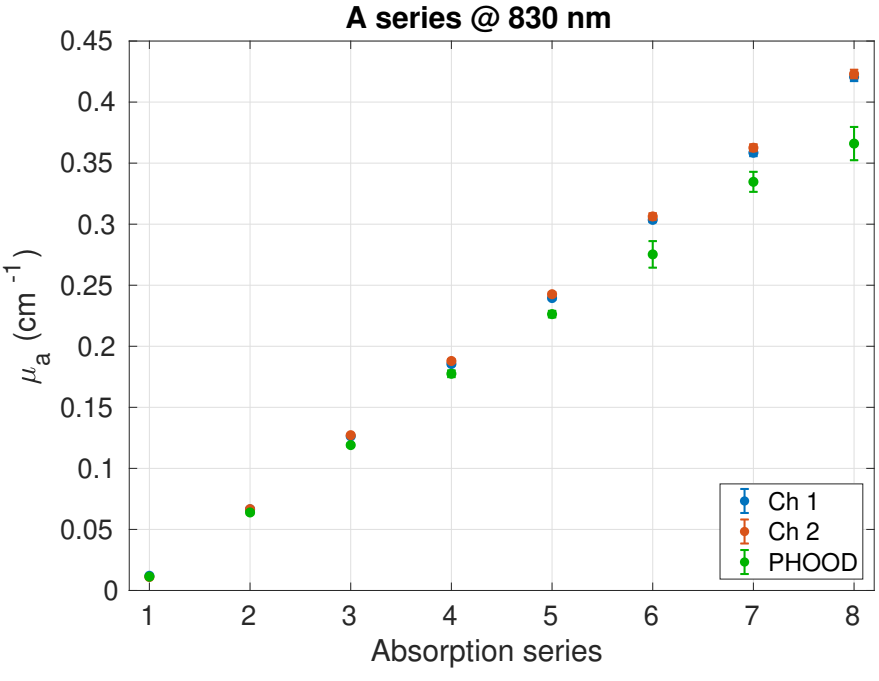

(b) μ_a at $\lambda = 830\,\mathrm{nm}$

Figure 3.6: Values of μ_a of the phantoms of the MEDPHOT A series measured by each channel and by the PHOOD instrument.

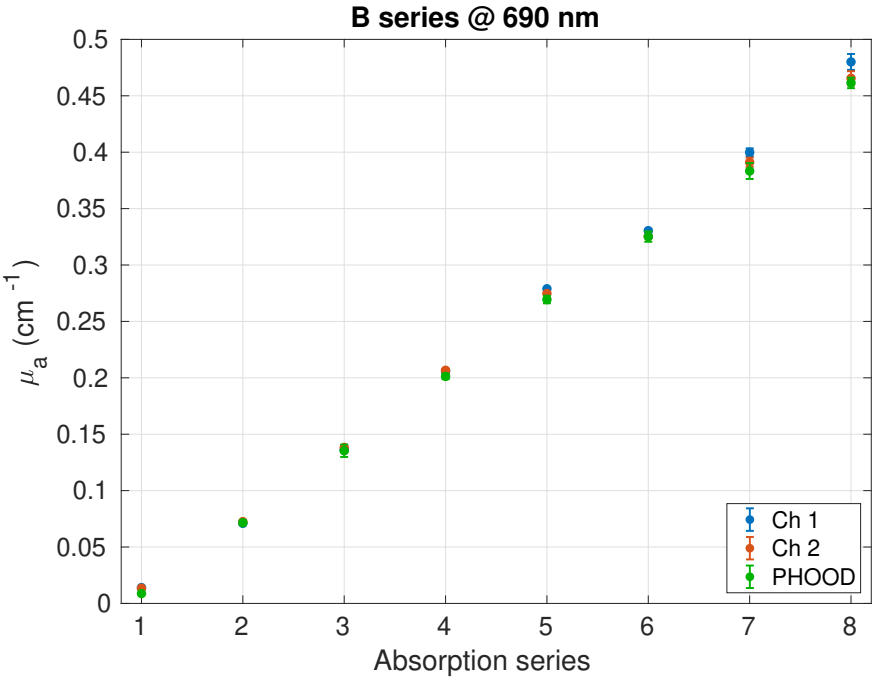

(a) μ_a at $\lambda = 690\,\mathrm{nm}$

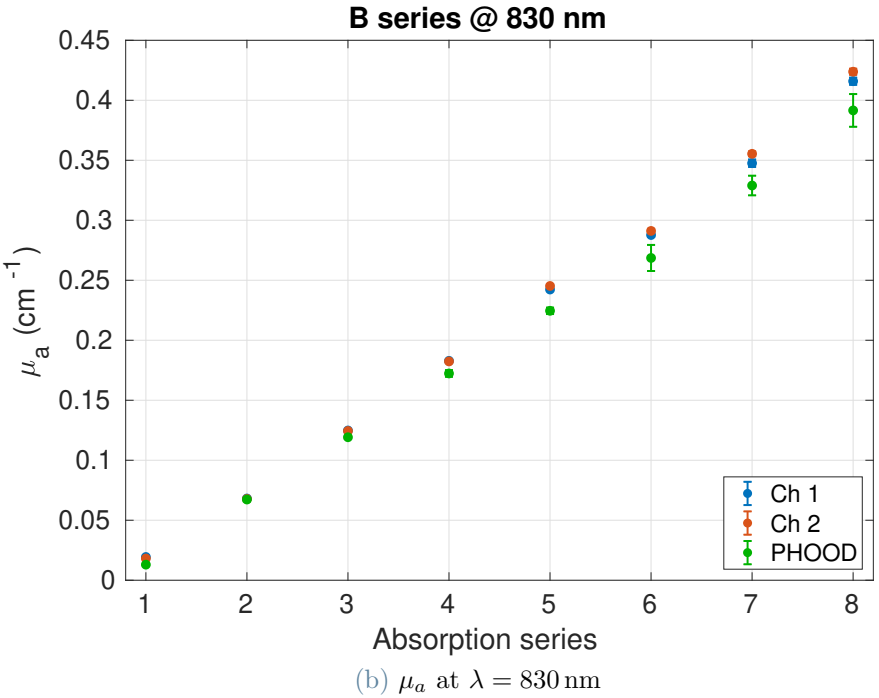

(b) μ_a at $\lambda = 830\,\mathrm{nm}$

Figure 3.7: Values of μ_a of the phantoms of the MEDPHOT B series measured by each channel and by the PHOOD instrument.

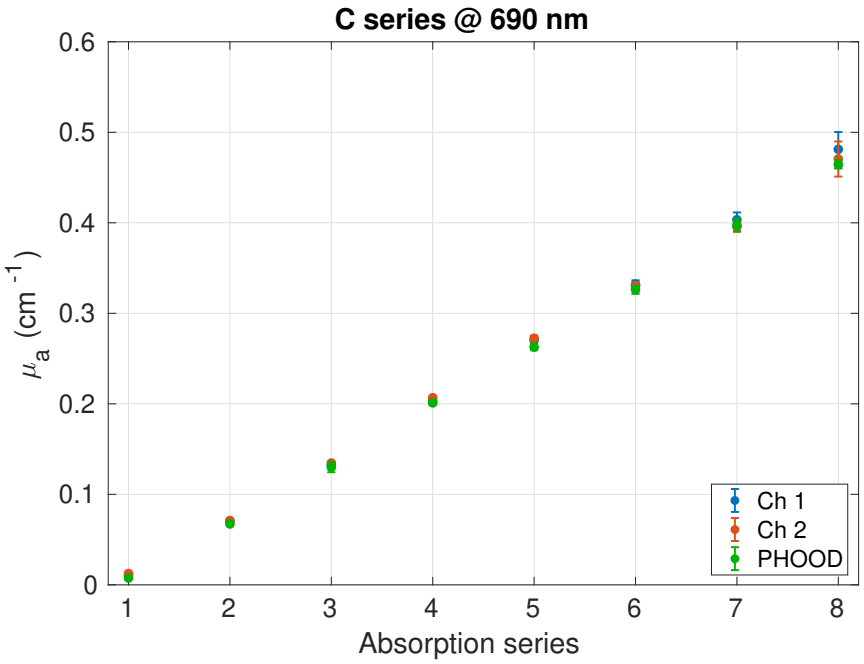

(a) μ_a at $\lambda = 690\,\mathrm{nm}$

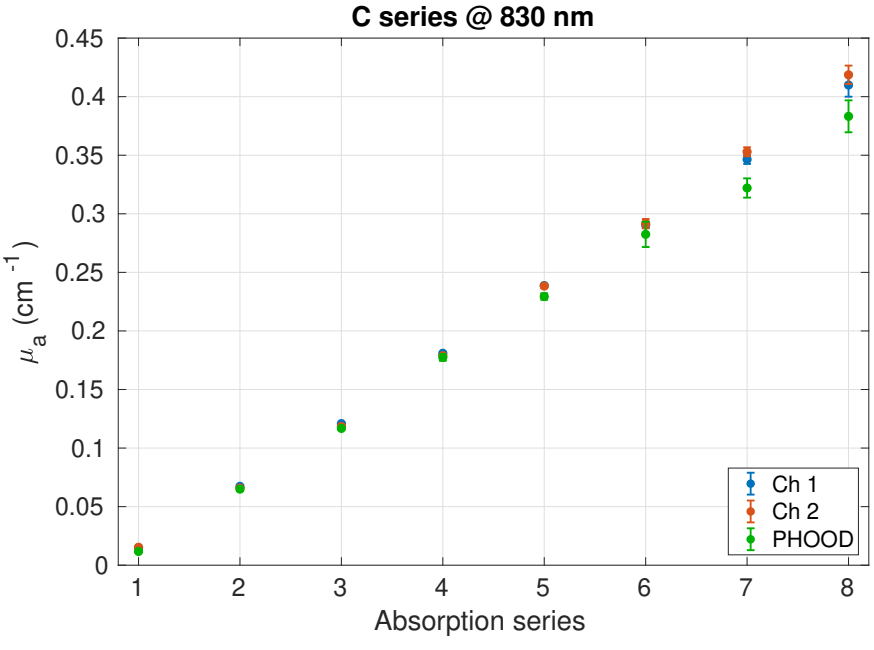

(b) μ_a at $\lambda = 830\,\mathrm{nm}$

Figure 3.8: Values of μ_a of the phantoms of the MEDPHOT C series measured by each channel and by the PHOOD instrument.

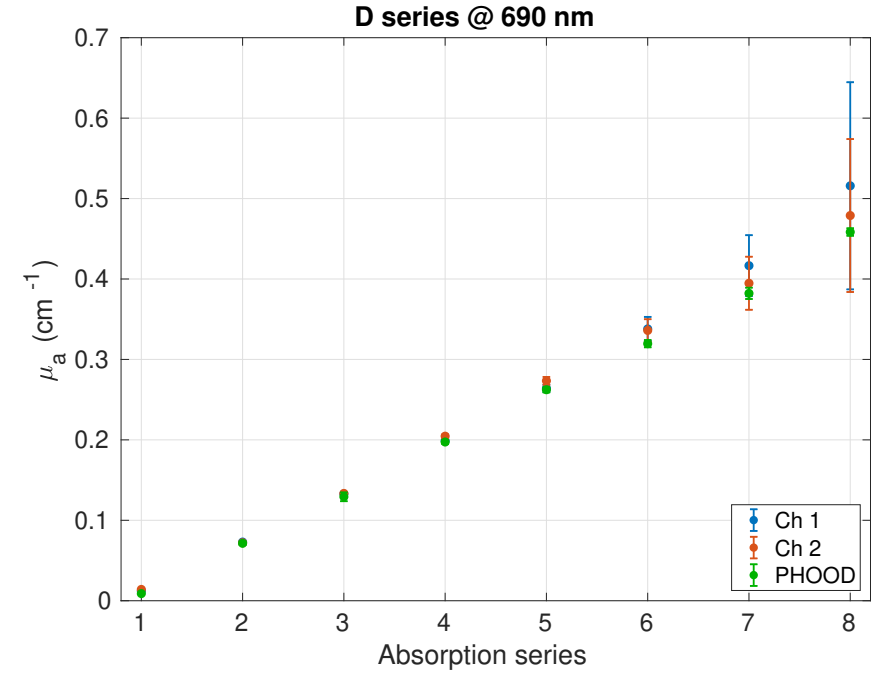

(a) μ_a at $\lambda = 690\,\mathrm{nm}$

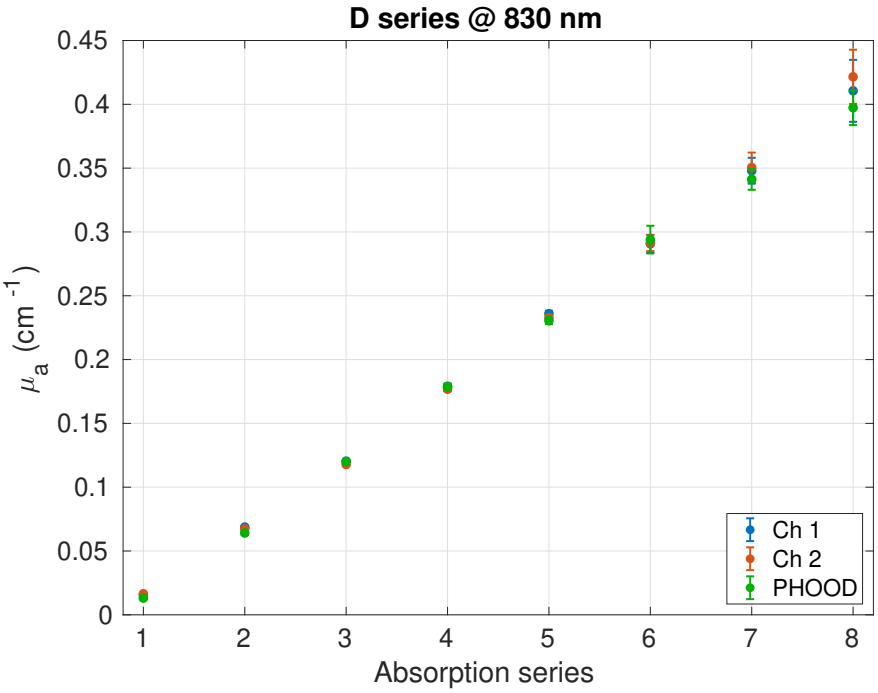

(b) μ_a at $\lambda = 830\,\mathrm{nm}$

Figure 3.9: Values of μ_a of the phantoms of the MEDPHOT D series measured by each channel and by the PHOOD instrument.

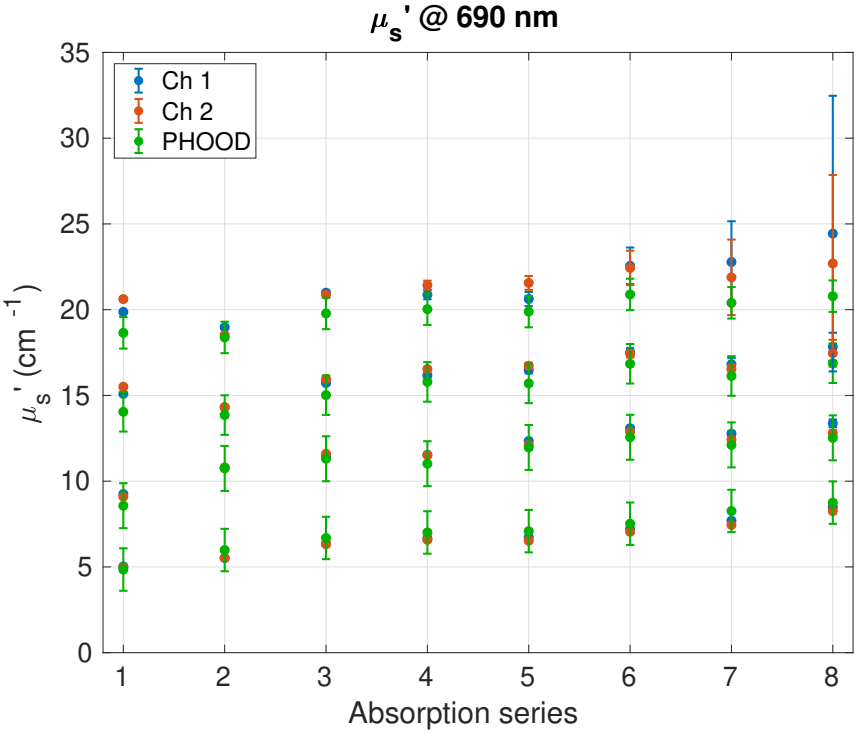

(a) μ_s' at $\lambda = 690\,\mathrm{nm}$

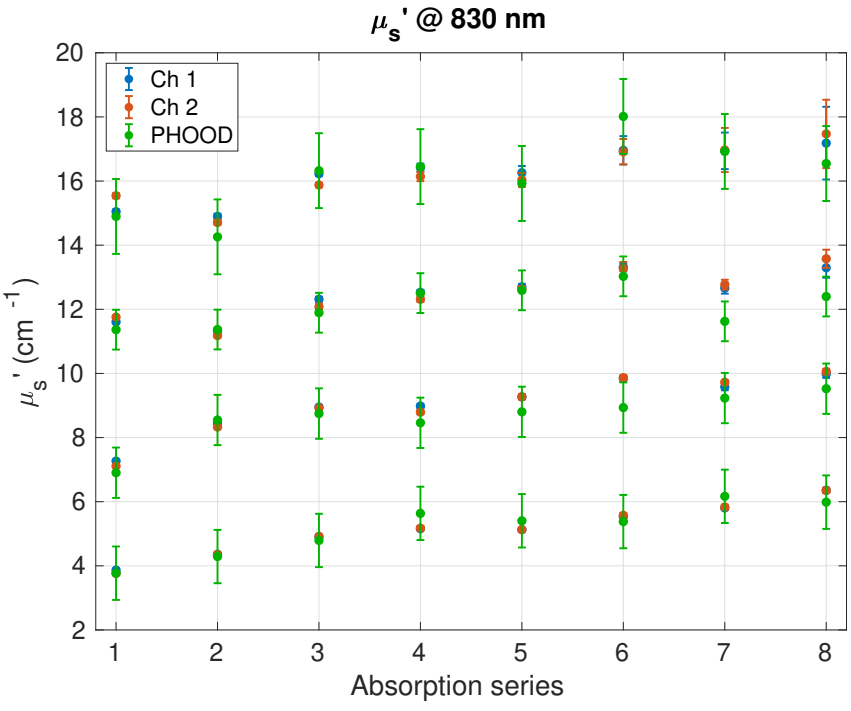

(b) μ_s' at $\lambda = 830\,\mathrm{nm}$

Figure 3.10: Values of μ_s' of the MEDPHOT phantoms measured by each channel and by the PHOOD instrument.

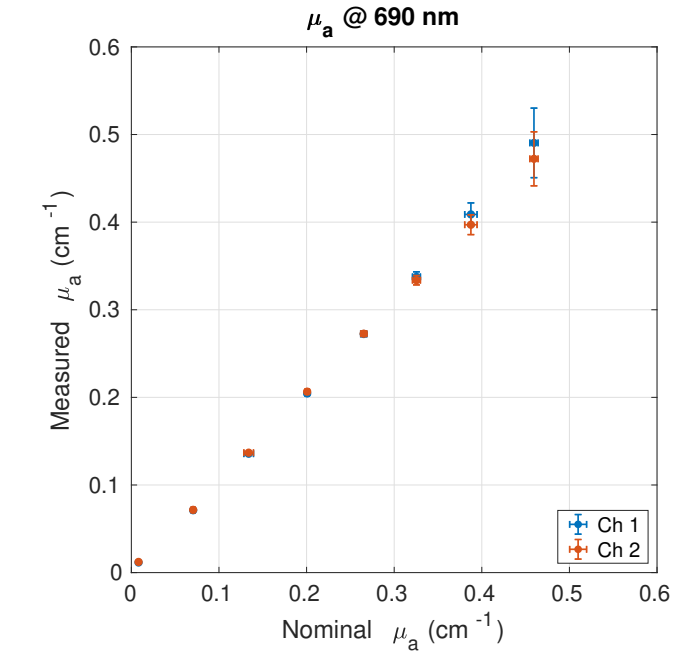

(a) μ_a at $\lambda = 690\,\mathrm{nm}$

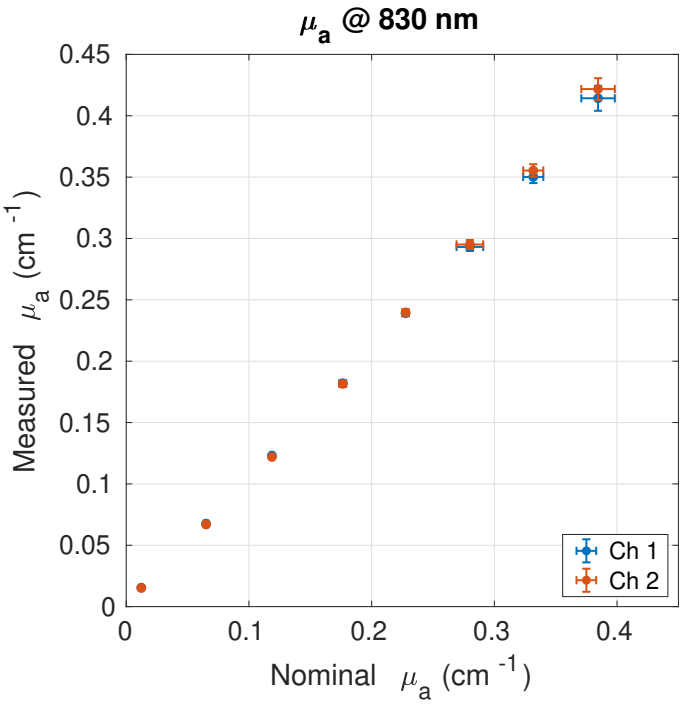

(b) μ_a at $\lambda = 830\,\mathrm{nm}$

Figure 3.11: Values of μ_a of the MEDPHOT phantoms measured by each channel plotted against the ones yielded by the PHOOD instrument.

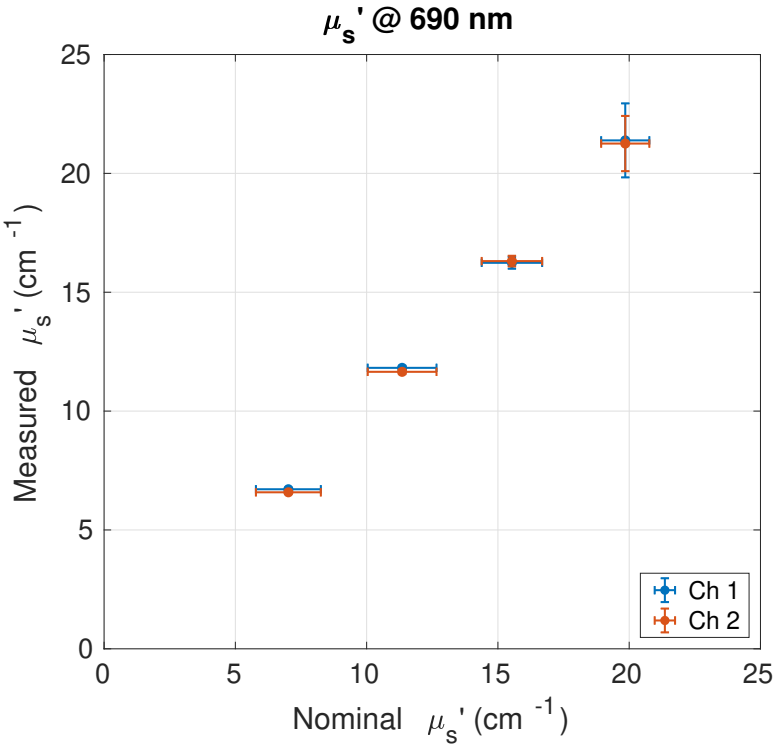

(a) μ_s' at $\lambda = 690\,\mathrm{nm}$

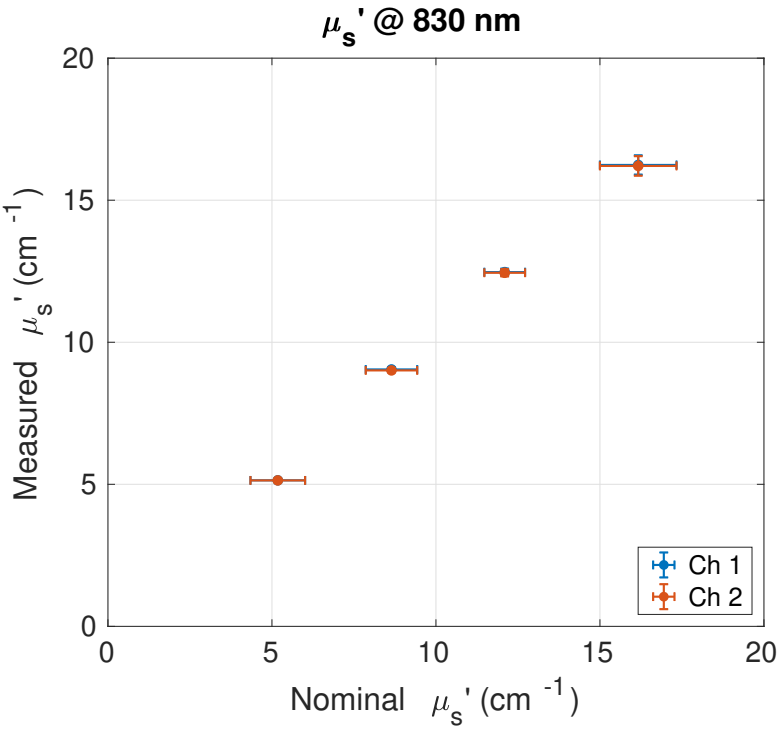

(b) μ_s' at $\lambda = 830\,\mathrm{nm}$

Figure 3.12: Values of μ_s' of the MEDPHOT phantoms measured by each channel plotted against the ones yielded by the PHOOD instrument.

Table 3.1: Relative errors of μ_a and μ'_s measured by the NIRSBOX vs the multi-wavelength PHOOD instrument

(a) Error on μ_a

Absorption series	Relative error (%)			
	690 nm		830 nm	
	Channel 1	Channel 2	Channel 1	Channel 2
1	40.9	48.7	25.9	23.9
2	0.9	1.5	4.0	2.9
3	1.3	2.2	3.7	2.7
4	1.9	2.9	3.2	2.9
5	2.7	2.8	5.0	5.3
6	3.7	2.6	4.6	5.4
7	5.5	2.4	5.5	7.1
8	6.7	2.8	7.7	9.7
Average (2-6)	2.1	2.4	4.1	3.8

(b) Error on μ'_s

Scattering series	Relative error (%)			
	690 nm		830 nm	
	Channel 1	Channel 2	Channel 1	Channel 2
A	4.4	6.2	0.7	0.8
B	4.1	2.7	4.6	4.2
C	4.5	5.0	3.1	2.9
D	7.7	7.1	0.5	0.2
Average	5.2	5.2	2.2	2.0

3.2. Comparison among autocorrelation algorithms

As for the DCS module, a set of measurements were carried out in order to compare the performance of the following methods of calculating the autocorrelation curves:

1. Classic multi-tau autocorrelation algorithm (detailed on page 29).
2. Asynchronous autocorrelation algorithm (detailed on page 30).
3. FFT-based autocorrelation algorithm (detailed on page 31).
4. Autocorrelation algorithm provided by the API of the time-tagger.
5. Hardware correlator (ALV-7004/USB-FAST by ALV GmbH) installed on a previously built DCS instrument [21] that uses the same laser source, fibers and detectors as the one developed in this work. The correlator implements the classic multi-tau algorithm with $P = 16$ registers and a binning ratio $m = 2$, and has a temporal resolution of 3 ns.

The algorithms were compared in terms of speed, stability and capability of following variations of the autocorrelation curves due to different factors.

The stability measurement was carried out in order to gauge the fluctuations of the D_B and β parameters over a long measurement time. The lower the amplitude of these oscillations, the more reliable the algorithm is on a single measurement.

As shown in fig. 1.2a on page 19, the autocorrelation curve exhibits different decays for different values of the diffusion coefficient. This parameter in turn depends on temperature and viscosity, according to the Einstein relation [30]:

$$D_B = \frac{k_B T}{6\pi r \eta} \tag{3.1}$$

where k_B is the Boltzmann constant, T the absolute temperature, r the radius of the scattering particles and η the dynamic viscosity of the solution. In order to test how well the algorithms can follow variations of the correlation curve, measurements on phantoms with different viscosities were carried out. The effect of T was instead not investigated, since at higher temperatures the phantoms behave irregularly due to chemical changes in their constituents.

On top of depending on D_B, the decay of the autocorrelation also depends on the source-detector separation, as shown in fig. 1.2b on page 19. Measurements at different inter-fiber distances were therefore carried out as well.

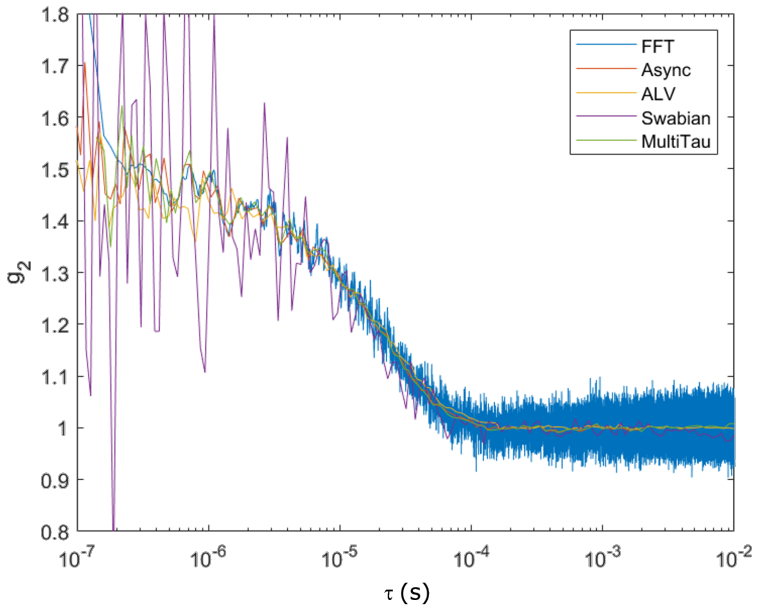

Figure 3.13: Example of autocorrelation curves calculated with the five different algorithms

For the first three algorithms, the raw arrival times of the photons were saved during the measurement and a MATLAB (Mathworks, Inc.) software later calculated the autocorrelations in post-processing. The other two acted instead in real time, processing data on-the-fly during the measurement. The photon count rate was the same in all the experiments.

Figure 3.13 shows an example of the curves obtained with the aforementioned algorithms. It can be noticed that they all exhibit approximately the same decay, but different levels of noise. In particular, the autocorrelation calculated by the time-tagger (purple curve) is much noisier than the other ones, especially for small values of τ. The FFT curve (blue) has many more data points ($\sim 5 \times 10^7$) than the other ones (~ 200), and these points become denser on the logarithmic axis for higher values of the time delay. This effect, which causes the noisy tail, is due to the linearly spaced values of τ used by the FFT algorithm.

As for time performance, the asynchronous algorithm proved to be the fastest one, taking about $0.6 \div 1.0$ s per curve for a count rate of 150 kHz. Each curve took $5 \div 7$ s to be calculated with the FFT-based algorithm, while the classic multi-tau one was the slowest, taking $150 \div 180$ s. It should be noted however that these times strongly depend on the computational power of the PC used, so they should not be viewed as absolute. Rather, it is their ratio that is significant and allows to compare the speeds of the various algorithms.

3.2.1. Stability measurement

The first measurement that was performed was a stability one. The goal was to assess the coefficients of variation of both D_B and β, that is, the ratios between the standard deviations and the averages of these quantities over the whole measurement time: $\mathrm{CV}(x) = \sigma(x)/\langle x \rangle$

The measurement lasted for 300 s, with integration time 1 s (one correlation curve calculated every second). The phantoms used were composed of distilled water, Intralipid and black India ink. The relative concentrations of Intralipid and ink were chosen so as to mimic typical values of optical parameters in human tissue ($\mu_s' \simeq 10\,\mathrm{cm}^{-1}$, $\mu_a \simeq 0.1\,\mathrm{cm}^{-1}$). The inter-fiber distance was set to 1.5 cm and a single detection channel was used. The photon count rate during the measurement was about 150 kHz.

The average value of D_B retrieved by fitting the different autocorrelation curves is plotted in fig. 3.14. As can be seen, the autocorrelation provided by the time-tagger has the worst stability, with an error bar spanning one order of magnitude upward. Moreover, its average value is much higher than the one obtained with the other algorithms. As for the other algorithms, as shown in fig. 3.14b they all yield compatible values of D_B, with relatively low variations.

Figure 3.15 shows the average value of β retrieved by analyzing the different curves. Rather than coming from a fitting procedure, as explained in section 2.1.2 this parameter was obtained directly from the data as $\beta = g_2(0) - 1$, and $g_2(0)$ was estimated as the average of the first few data points. Again, the algorithm of the time-tagger shows the highest variability; this is in line with what was already observed in fig. 3.13: the Swabian curve is much noisier than the other ones in the region used to estimate β. Nevertheless, all the curves show approximately the same value of β, in line with the fact that they all have similar values for low time delays τ.

The coefficients of variation of both D_B and β for the various algorithms are plotted in figs. 3.16 and 3.17. The data relative to the time-tagger have been omitted for clarity, since as already observed both values are much higher than the ones of the other algorithms. As for D_B (fig. 3.16), all values are lower than 5% except for the FFT. This is likely due to the difficulty in finding the right fitting interval for its curve, due to the linearity of the time bins and abundance of data points. The situation is different for the CVs of β (fig. 3.17), which are all similar to one another. This is in line with the corresponding curves of fig. 3.13 having similar fluctuations for low time delays. Finally, in all cases the CV of β is lower than the one of D_B. Indeed, the value of β is retrieved directly from the curves, with a procedure that is more robust than fitting.

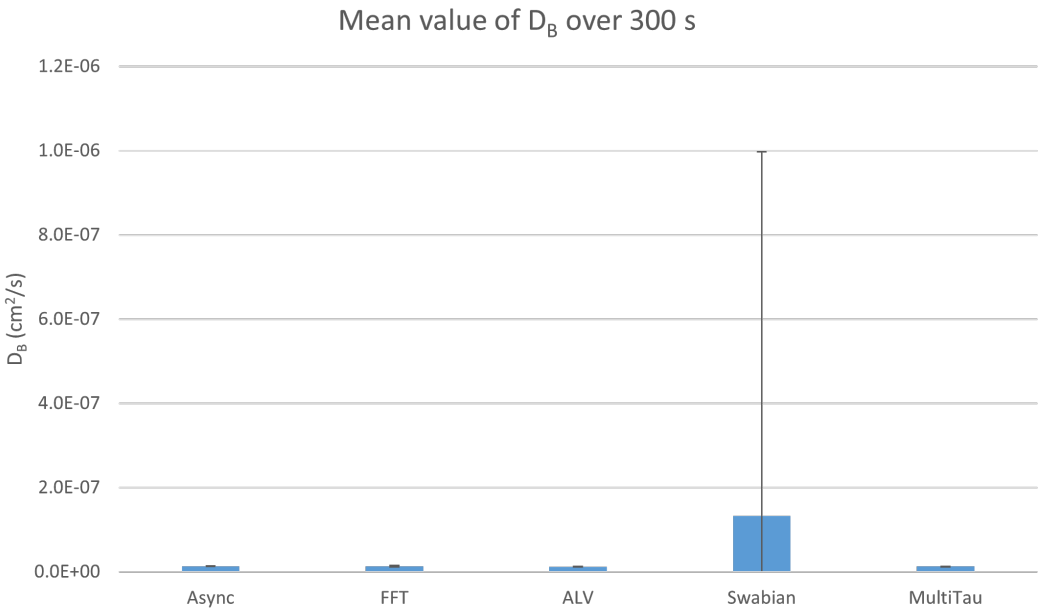

(a) All algorithms

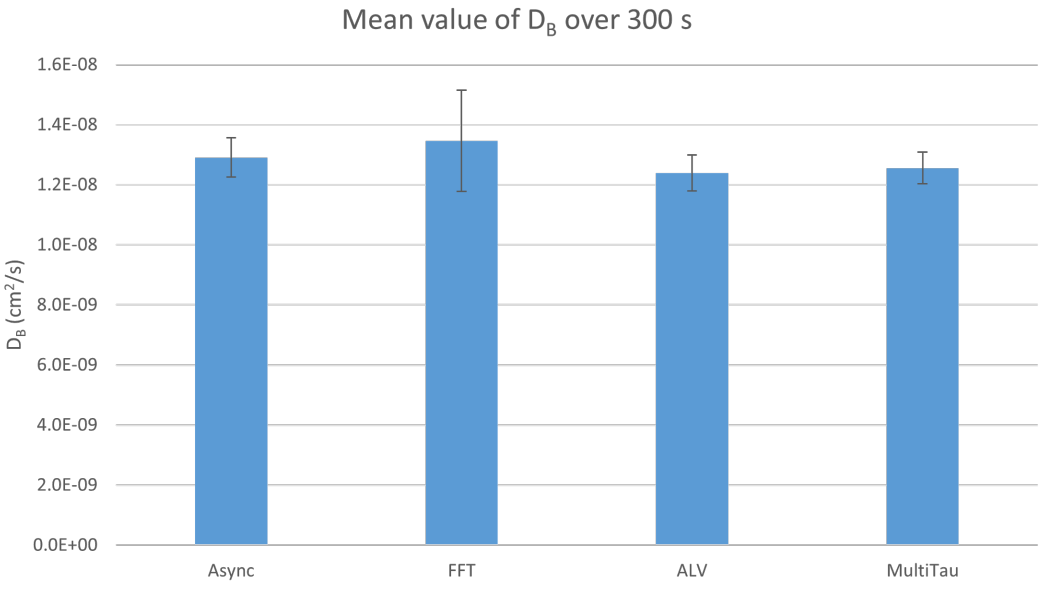

(b) Without Swabian

Figure 3.14: Average value of the diffusion coefficient D_B over the whole stability measurement yielded by the different algorithms

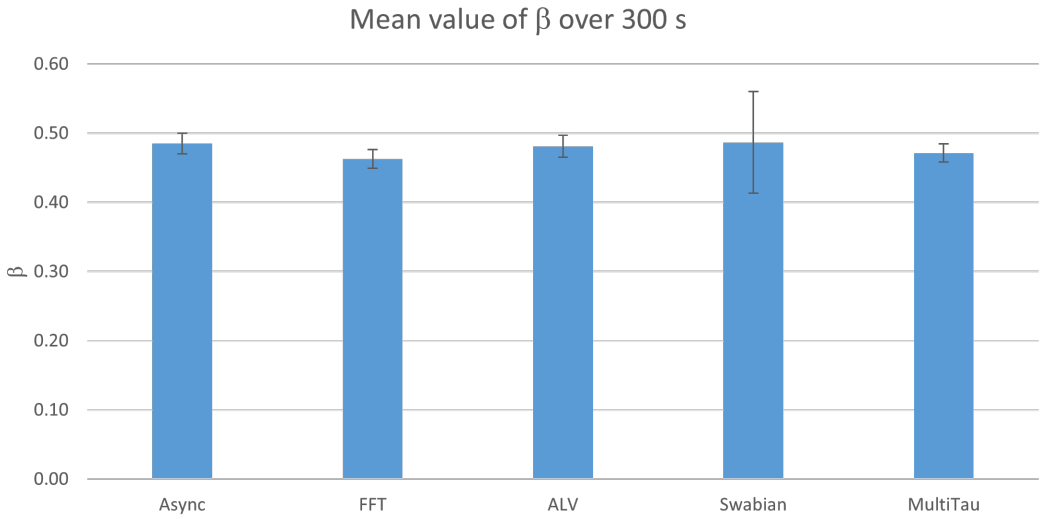

Figure 3.15: Average value of the parameter β over the whole stability measurement yielded by the different algorithms

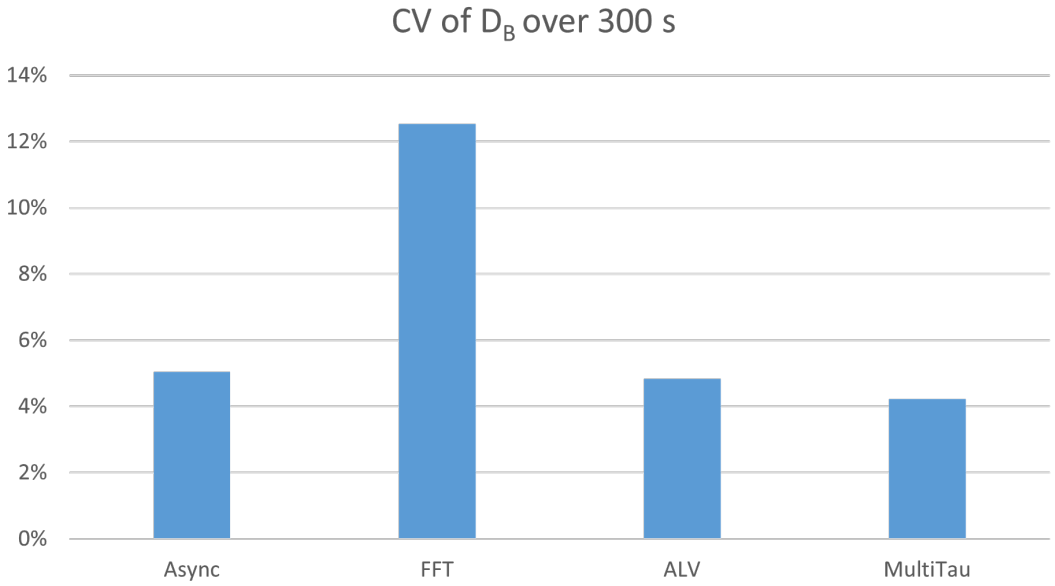

Figure 3.16: Coefficient of variation of D_B over the stability measurement relative to the various algorithms (Swabian excluded)

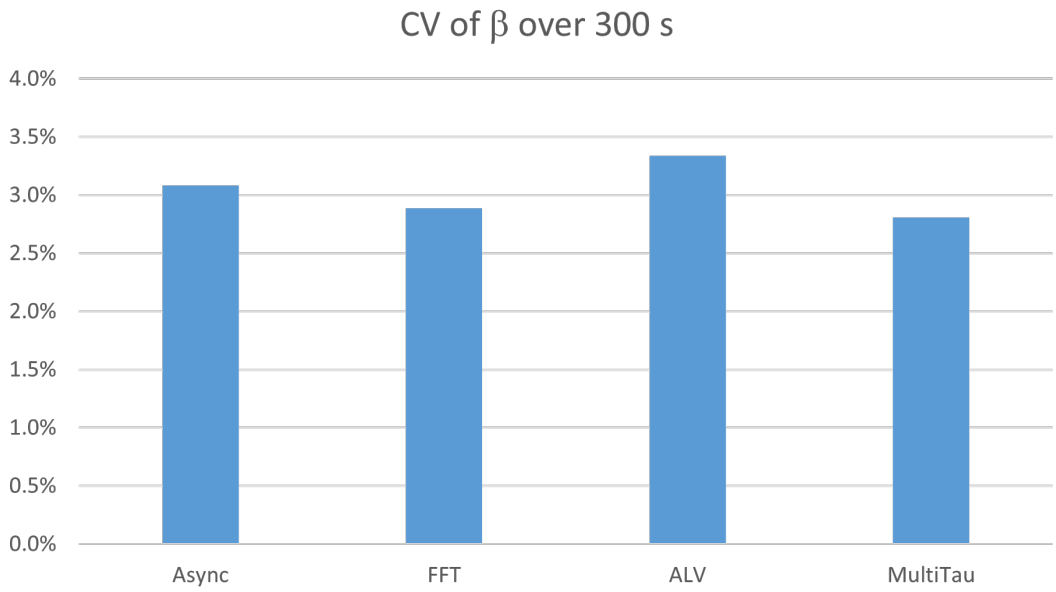

Figure 3.17: Coefficient of variation of β over the stability measurement relative to the various algorithms (Swabian excluded)

3.2.2. Variable viscosity

In the second measurement four different phantoms were employed, each one containing a different concentration of glycerol (from 0% to 30%, in steps of 10%). Glycerol affects the dynamic viscosity η of the solution, which in turn changes the value of the Brownian diffusion coefficient according to eq. (3.1). In particular, by increasing the glycerol concentration the viscosity η increases, so we expect lower values of D_B. The goal of the measurement was to assess how well the different algorithms are able to follow the variations of D_B caused by the different viscosities.

Each phantom was measured for 30 s, with integration time 1 s. The inter-fiber distance was set to 1.5 cm and a single detection channel was used. The count rate was about 150 kHz for all phantoms.

The average values of D_B and β are shown in fig. 3.18. As can be seen in fig. 3.18a, all algorithms except for the time-tagger one are able to detect the decrease of D_B caused by the increasing concentrations of glycerol. On top of showing the highest variability, the algorithm implemented by the time-tagger is also wildly inaccurate at times, yielding values of D_B that are one order of magnitude greater than the others for the phantoms with 0% and 30% glycerol concentration (not shown on the plot). All algorithms give similar values of β (fig. 3.18b), with the classic multi-tau algorithm providing the smallest one and the FFT and time-tagger the highest across all phantoms.

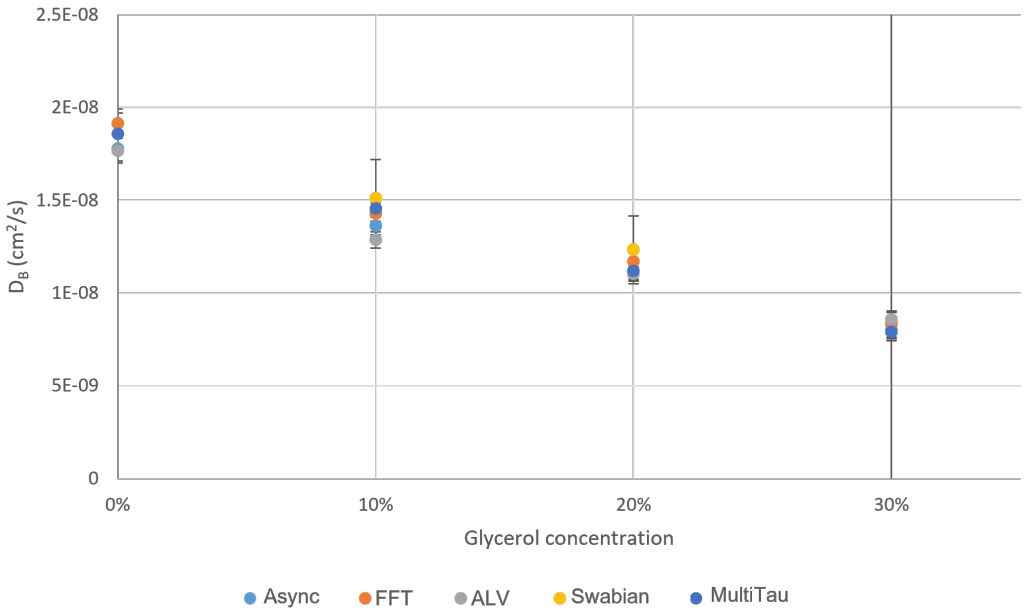

(a) Average D_B

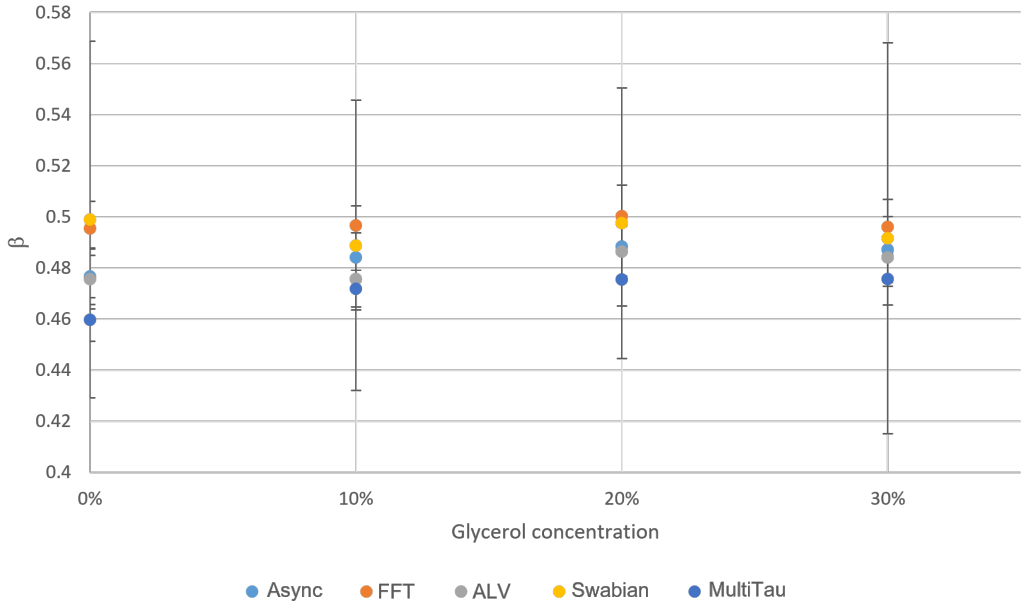

(b) Average β

Figure 3.18: Average values of D_B and β yielded by the different algorithms for the various levels of viscosity

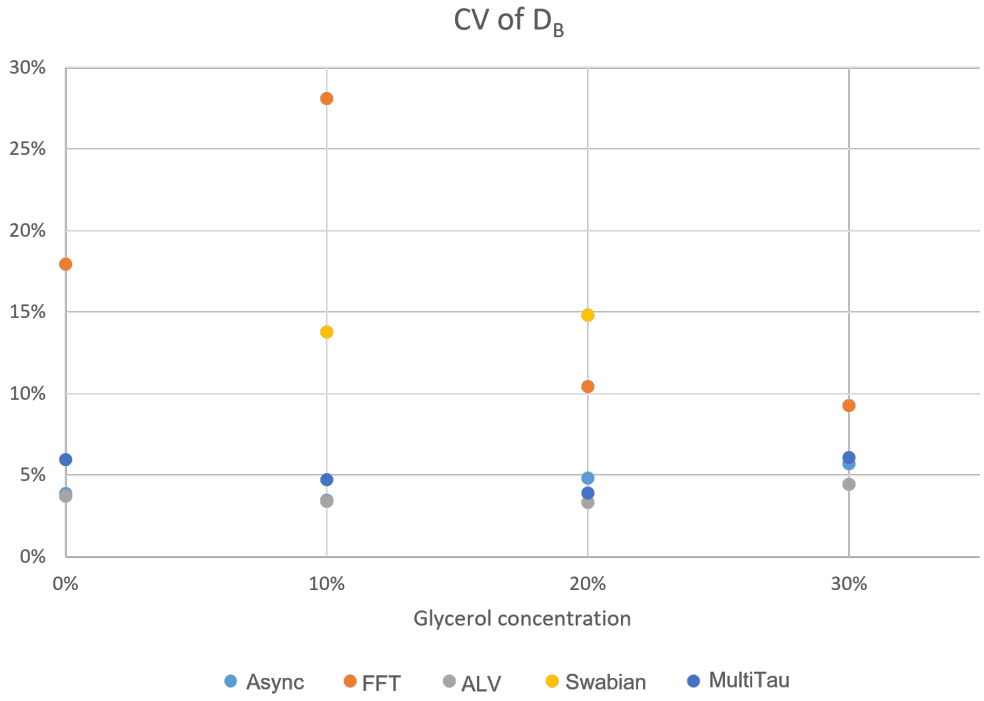

(a) CV of D_B

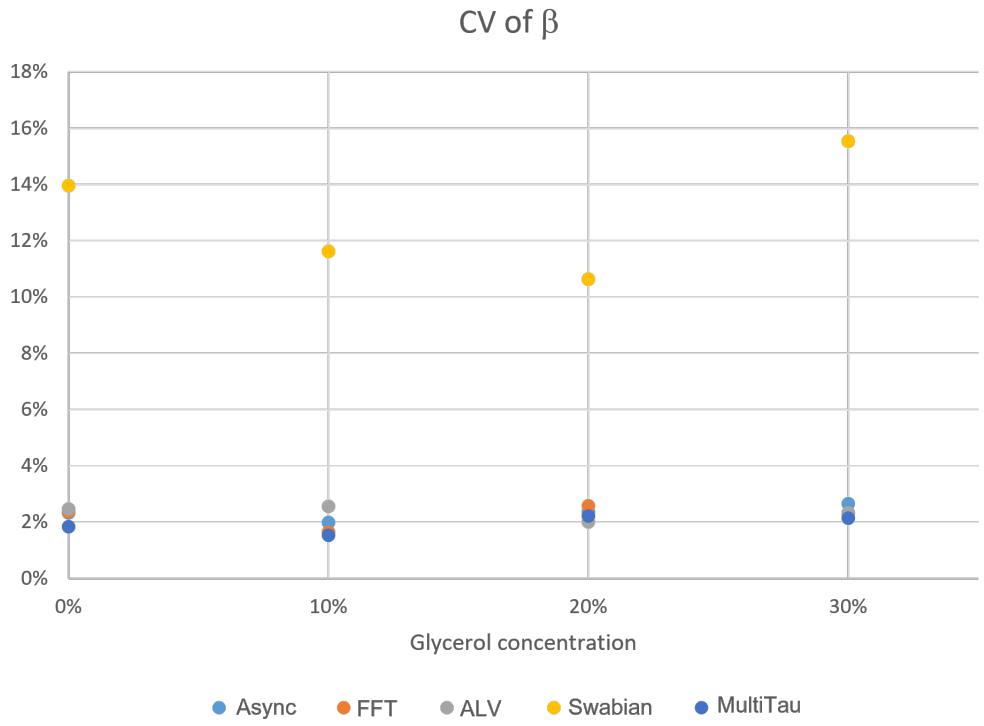

(b) CV of β

Figure 3.19: Coefficients of variation of D_B and β yielded by the different algorithms for the various levels of viscosity

The coefficients of variation for both D_B and β are plotted in fig. 3.19. Figure 3.19a shows that the FFT and time-tagger algorithms exhibit the highest variabilities (for the 0% and 30% phantoms the time-tagger CV is $\simeq 500\%$). All the other algorithms have an error of about 5%, with the hardware correlator staying consistently below this threshold. As for β (fig. 3.19b), all algorithms consistently show stabilities within 3% across all phantoms, except the time-tagger one, whose CV is always higher than 10%.

3.2.3. Variable source-detection separation

Finally, a measurement at varying inter-fiber distances was performed. As shown in fig. 1.2b on page 19, the further apart the injection and detection points are, the sooner the scattered light loses correlation. The goal of the measurement was to test how well each algorithm is able to follow such variation in the autocorrelation curve.

The phantom was measured for 30 s at each inter-fiber distance, with integration time 1 s. Three detection fibers were placed 1 cm, 1.5 cm and 2 cm away from the injection point, respectively and were connected to three detectors. The count rate was 150 kHz.

The average values of D_B and β retrieved are plotted in figs. 3.20 and 3.21. Figure 3.20 shows that the time-tagger algorithm exhibits the highest variability for both D_B and β, overestimating the value of the former by one order of magnitude at the shortest inter-fiber distance. Figure 3.21 reports the same results for the other algorithms. As can be seen, the asynchronous, hardware and multi-tau correlations all agree on the value of D_B, which as expected is independent of the inter-fiber distance (fig. 3.21a). The FFT algorithm on the other hand yields a higher value; this discrepancy is likely due to the difficulty in fitting the data caused by the linearity of data points. As for β (fig. 3.21b), the hardware correlator consistently measures a lower value across all distances. This effect, which was not observed in the previous experiments, could be due to measurement problems. The other algorithms suggest an increase in β when the source-detector separation increases from 1 cm to 1.5 cm.

3.2.4. Conclusions

In light of the conducted experiments, the time-tagger algorithm used in the setup is the worst in terms of both accuracy and precision among the investigated ones. It has however the advantage of speed, being able to calculate the autocorrelation curves in real time. This makes it suitable for giving a first visualization of the data during the measurement, since it is able to follow at least qualitatively the variations of D_B.

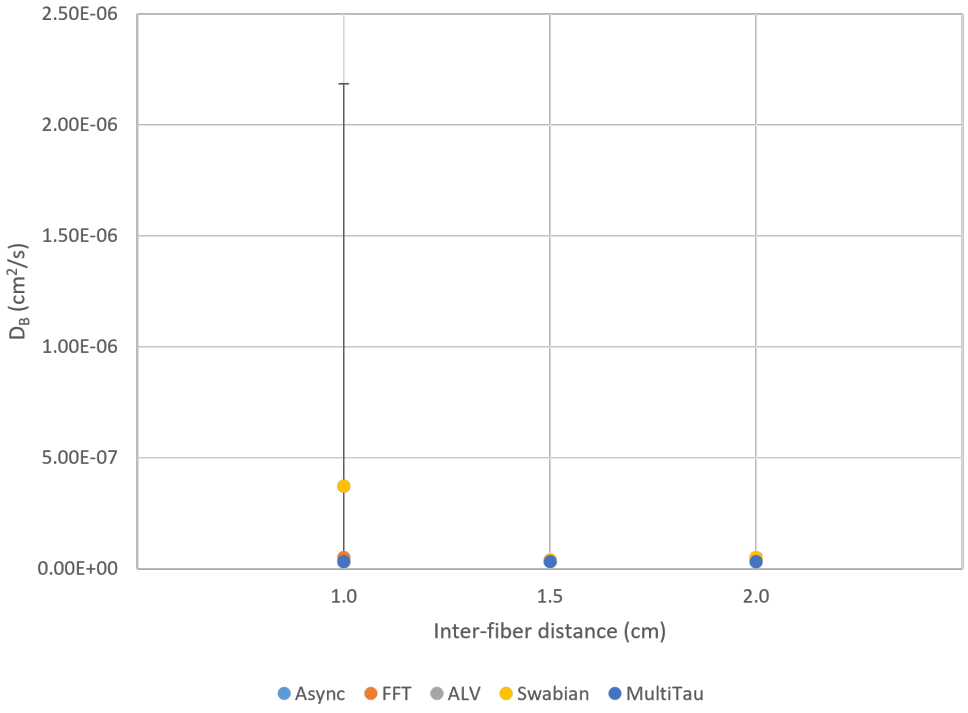

(a) Average value of D_B

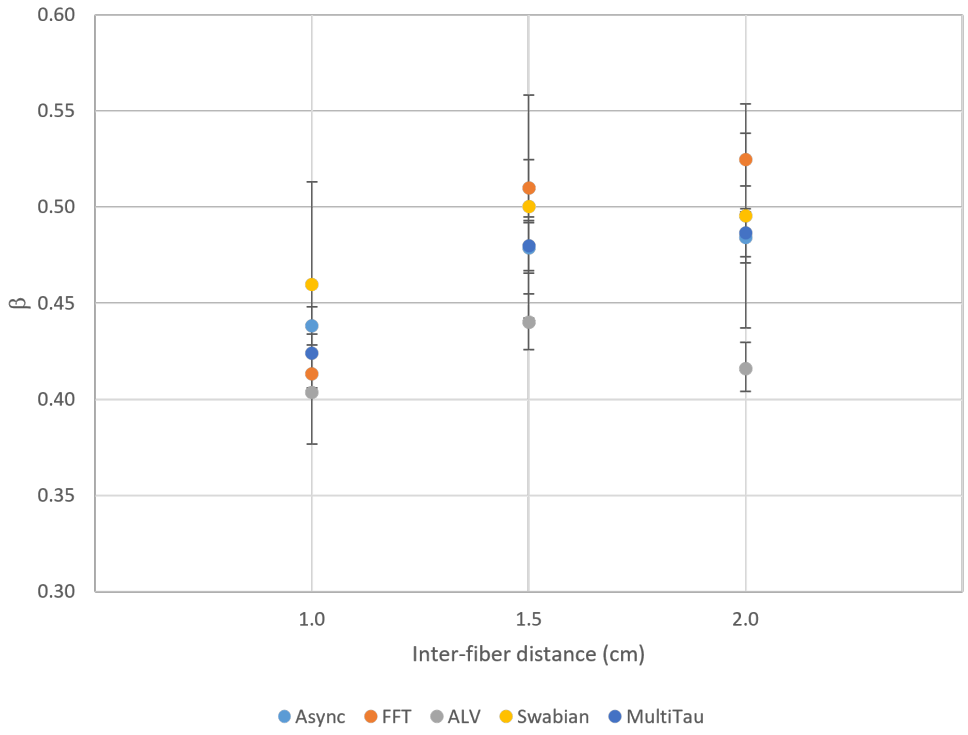

(b) Average value of β

Figure 3.20: Average values of D_B and β yielded by the different algorithms for the various inter-fiber distances

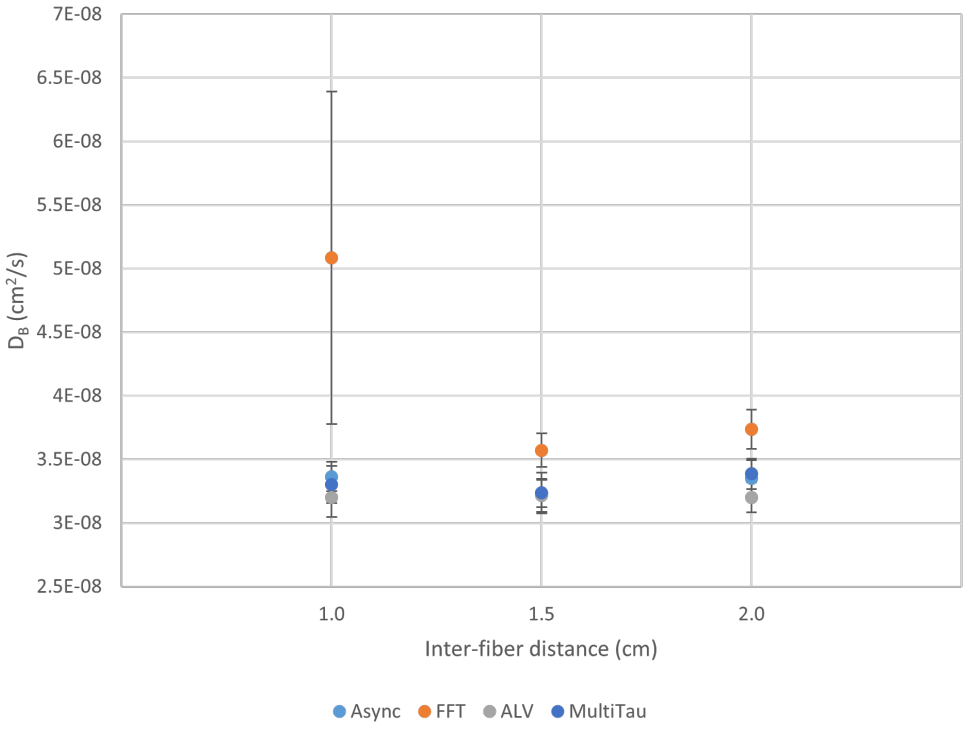

(a) Average value of D_B

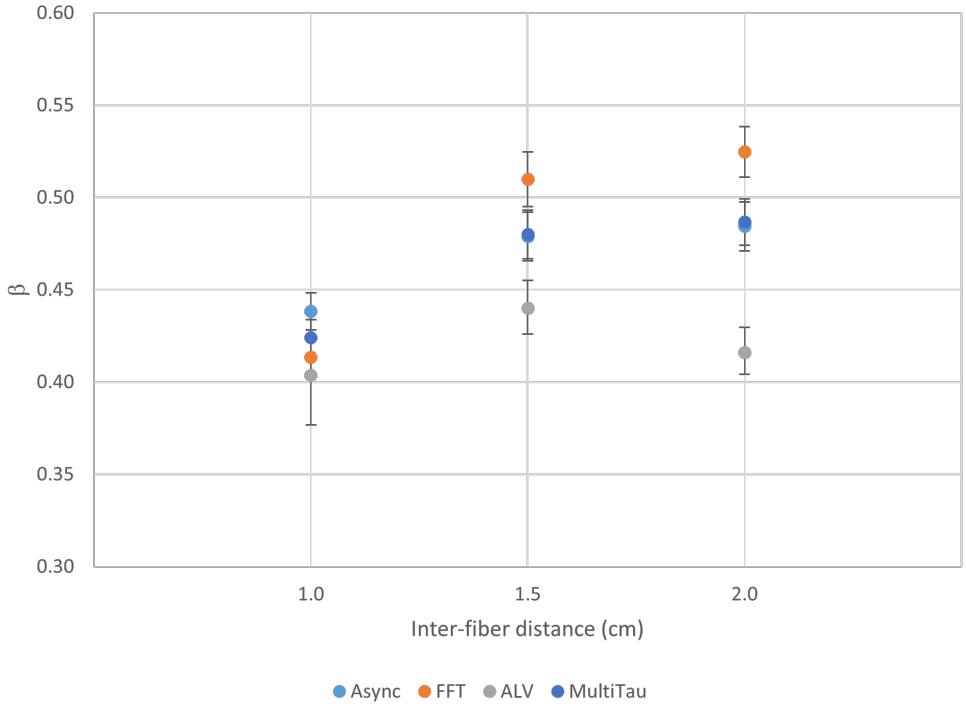

(b) Average value of β

Figure 3.21: Average values of D_B and β yielded by different algorithms (time-tagger omitted) for the various inter-fiber distances

For post-processing, where speed is not an issue, one of the other more precise and accurate algorithms should be preferred instead. The best candidates are the classic multi-tau and asynchronous ones, which perform similarly in terms of both accuracy and precision. In particular, while the classic algorithm sacrifices speed for accuracy, the asynchronous one is also rather fast, and with sufficiently powerful computational hardware could potentially be integrated in an experimental setup, to provide a real-time monitoring that is accurate and stable.

4 | Conclusions and future developments

"We can only see a short distance ahead,
but we can see plenty there that needs to be done"
– Alan Turing

This thesis work focused on the development and characterization of an innovative compact instrument for hemodynamic and metabolic measurements. The device makes use of non-invasive diffuse-optics techniques, namely NIRS (more precisely TRS) and DCS. In particular, NIRS allows the measurement of oxy- and deoxy-hemoglobin concentrations and tissue oxygen saturation, while DCS provides quantitative information on blood flow.

As for TRS, the device makes use of a state-of-the-art TD-NIRS system featuring two laser sources at different wavelengths, as well as two detection channels. The former feature is needed in order to measure the concentrations of oxy- and deoxy-hemoglobin in tissue, while the latter potentially allows to separate the contribution of the superficial layer from that of deeper tissue. The TRS module was assessed in terms of stability, linearity and accuracy. The stability measurement showed that the instrument reaches a stationary regime in 30 minutes, after which the mean values of the measured optical parameters remain constant. Additionally, their oscillations stay within 3% of the mean value the whole time. Finally, the two detectors yield the same values within a 2% margin. The linearity and accuracy measurements validated the instrument against a previously built one. They showed good agreement between the two devices, with the one developed in this thesis being closer to linearity in some cases. Overall, these results suggest that the device is suitable for both absolute and relative measurements.

Just like the NIRS module, the DCS one features multiple detection channels, bringing the same advantages already discussed to blood flow measurements as well. Alternatively, employing all detectors to collect the signal from the same point allows to reduce noise. Differently from previously built systems, which relied on dedicated hardware to calculate the autocorrelation, the one developed here makes use of a software algorithm to achieve

the same task. This ultimately allows for more flexibility, as well as holding potential for pre- and post-processing of the signal. Different algorithms were explored and compared in terms of stability as well as capability of following variations in sample viscosity and inter-fiber distance. The experiments showed that, though very fast, the algorithm provided by the time-tagging module built into the device is both inaccurate and extremely imprecise, making it a poor choice for anything but a qualitative visualization of the data during the measurement. On the other hand, the explored asynchronous multi-tau autocorrelation algorithm showed performance comparable to that of hardware correlators while still keeping computation time low. This makes it a great choice for analyzing the data not only in post-processing, but potentially in real-time too: a future version of the device could implement this algorithm in place of the time-tagger one.

In this thesis the TRS and DCS modules were designed and assessed separately, but to work as intended they ought to be integrated in the same instrument. The software that was developed to control the DCS components could then be expanded to govern the TRS one as well. This can be readily achieved through the DLLs that are available for the NIRSBOX. Additionally, issues such as the synchronization of the two modules and cross-talk of the laser sources would need to be addressed. It would then be possible to make the complete measurement of oxy-, deoxy- and total hemoglobin concentration, tissue oxygen saturation and blood flow index as well as visualize the data through a single interface.

The device developed in this thesis lends itself to several applications. A multi-distance system allows the implementation of a more complex multi-layer model in place of the simple homogeneous one. While the latter is more sensitive to superficial tissue, the former would allow to separate the contributions of deeper tissue from those of the top layers [31]. Multi-distance devices allow to investigate blood flow and oxygenation of skeletal muscles [32] (such as those of the arm and the leg) and head [31]. Besides blood flow, DCS allows to observe directly skeletal muscle contraction [33] and neuronal activity [34]: both of these applications require sub-second integration times, which are achievable thanks to the flexible software autocorrelator as well as the multiple detection channels, which allow to reach higher signal-to-noise ratios.

Bibliography

[1] Max Cutler. "Transillumination of the breast". In: *Annals of surgery* 93 (1 Jan. 1931), pp. 223–234. DOI: 10.1097/00000658-193101000-00032.

[2] T. Durduran et al. "Diffuse optics for tissue monitoring and tomography". In: *Reports on Progress in Physics* 73.7 (June 2010), p. 076701. DOI: 10.1088/0034-4885/73/7/076701.

[3] Agnese De Carli et al. "Cerebral oxygenation and blood flow in term infants during postnatal transition: BabyLux project". In: *Archives of Disease in Childhood - Fetal and Neonatal Edition* 104.6 (2019), F648–F653. DOI: 10.1136/archdischild-2018-316400.

[4] Rebecca Re et al. "Time Domain Near Infrared Spectroscopy Device for Monitoring Muscle Oxidative Metabolism: Custom Probe and In Vivo Applications". In: *Sensors* 18.1 (2018). DOI: 10.3390/s18010264.

[5] Alessandro Torricelli et al. "Time domain functional NIRS imaging for human brain mapping". In: *NeuroImage* 85 (2014), pp. 28–50. DOI: 10.1016/j.neuroimage.2013.05.106.

[6] Sergio Fantini and Angelo Sassaroli. "Near-infrared optical mammography for breast cancer detection with intrinsic contrast". In: *Annals of Biomedical Engineering* 40 (2012), pp. 398–407. DOI: 10.1007/s10439-011-0404-4.

[7] Turgut Durduran and Arjun G. Yodh. "Diffuse correlation spectroscopy for non-invasive, micro-vascular cerebral blood flow measurement". In: *NeuroImage* (2014), pp. 51–63. DOI: 10.1016/j.neuroimage.2013.06.017.

[8] Erin M. Buckley et al. "Diffuse correlation spectroscopy for measurement of cerebral blood flow: future prospects". In: *Neurophotonics* 1.1 (2014), p. 011009. DOI: 10.1117/1.NPh.1.1.011009.

[9] David R. Busch et al. "Detection of Brain Hypoxia Based on Noninvasive Optical Monitoring of Cerebral Blood Flow with Diffuse Correlation Spectroscopy". In: *Neurocritical care* 30.1 (Feb. 2019), pp. 72–80. DOI: 10.1007/s12028-018-0573-1.

[10] Martina Giovannella et al. "BabyLux device: a diffuse optical system integrating diffuse correlation spectroscopy and time-resolved near-infrared spectroscopy for the

neuromonitoring of the premature newborn brain". In: *Neurophotonics* 6.2 (2019), p. 025007. DOI: 10.1117/1.NPh.6.2.025007.

[11] Fabrizio Martelli et al. *Light Propagation through Biological Tissue and Other Diffusive Media*. Jan. 2010. ISBN: 978-0-8194-7658-6.

[12] Craig F. Bohren and Donald R. Huffman. *Absorption and Scattering of Light by Small Particles*. John Wiley & Sons, Ltd, 1998. ISBN: 9783527618156. DOI: 10.1002/9783527618156.

[13] Irving J. Bigio and Sergio Fantini. *Quantitative Biomedical Optics: Theory, Methods, and Applications*. Cambridge Texts in Biomedical Engineering. Cambridge University Press, 2016. DOI: 10.1017/CBO9781139029797.

[14] B. H. Armstrong and R. W. Nicholls. *Emission, Absorption, and Transfer of Radiation in Heated Atmospheres*. Elsevier Science & Technology, 1972.

[15] Thomas G. Mayerhöfer, Harald Mutschke, and Jürgen Popp. "Employing Theories Far beyond Their Limits – The Case of the (Boguer-) Beer-Lambert Law". In: *ChemPhysChem* 17.13 (2016), pp. 1948–1955. DOI: 10.1002/cphc.201600114.

[16] Milton Kerker. *The Scattering of Light and other Electromagnetic Radiation*. Physical chemistry 16. Literaturverz. S. 620 - 645. New York: Acad. Press, 1969. XV, 666. ISBN: 0124045502.

[17] Akira Ishimaru. *Wave Propagation and Scattering in Random Media. Akira*. Vol. 1. Single scattering and transport theory. New York: Academic Press, 1978. XV, 250. ISBN: 0123747015.

[18] Elmer Eugene Lewis. *Computational methods of neutron transport*. New York: Wiley, 1984. XVI, 401. ISBN: 0471092452.

[19] James Johnson Duderstadt and William Russell Martin. *Transport theory*. Wiley, 1979. ISBN: 047104492X.

[20] Raphael Aronson. "Boundary conditions for diffusion of light". In: *J. Opt. Soc. Am. A* 12.11 (Nov. 1995), pp. 2532–2539. DOI: 10.1364/JOSAA.12.002532.

[21] Caterina Amendola et al. "A Compact Multi-Distance DCS and Time Domain NIRS Hybrid System for Hemodynamic and Metabolic Measurements". In: *Sensors* 21.3 (2021). DOI: 10.3390/s21030870.

[22] Fabrizio Martelli et al. "Method for measuring the diffusion coefficient of homogeneous and layered media". In: *Opt. Lett.* 25.20 (Oct. 2000), pp. 1508–1510. DOI: 10.1364/OL.25.001508.

[23] Fabrizio Martelli, Samuele Del Bianco, and Giovanni Zaccanti. "Procedure for retrieving the optical properties of a two-layered medium from time-resolved reflectance measurements". In: *Opt. Lett.* 28.14 (July 2003), pp. 1236–1238. DOI: 10.1364/OL.28.001236.

[24] Jing Dong et al. “Diffuse correlation spectroscopy with a fast Fourier transform-based software autocorrelator”. In: *Journal of Biomedical Optics* 17.9 (2012), pp. 1–9. DOI: 10.1117/1.JBO.17.9.097004.

[25] Michele Lacerenza et al. “Wearable and wireless time-domain near-infrared spectroscopy system for brain and muscle hemodynamic monitoring”. In: *Biomed. Opt. Express* 11.10 (Oct. 2020), pp. 5934–5949. DOI: 10.1364/BOE.403327.

[26] Davide Magatti and Fabio Ferri. “Fast multi-tau real-time software correlator for dynamic light scattering”. In: *Appl. Opt.* 40.24 (Aug. 2001), pp. 4011–4021. DOI: 10.1364/AO.40.004011.

[27] Michael Wahl et al. “Fast calculation of fluorescence correlation data with asynchronous time-correlated single-photon counting”. In: *Opt. Express* (Dec. 2003), pp. 3583–3591. DOI: 10.1364/OE.11.003583.

[28] Fangzhou Zhao et al. “Reproducibility of identical solid phantoms”. In: *Journal of Biomedical Optics* 27.7 (2022), p. 074713. DOI: 10.1117/1.JBO.27.7.074713.

[29] Antonio Pifferi et al. “Performance assessment of photon migration instruments: the MEDPHOT protocol”. In: *Appl. Opt.* 44.11 (Apr. 2005), pp. 2104–2114. DOI: 10.1364/AO.44.002104.

[30] A. Einstein. “Über die von der molekularkinetischen Theorie der Wärme geforderte Bewegung von in ruhenden Flüssigkeiten suspendierten Teilchen”. In: *Annalen der Physik* 322.8 (1905), pp. 549–560. DOI: 10.1002/andp.19053220806.

[31] Louis Gagnon et al. “Investigation of diffuse correlation spectroscopy in multi-layered media including the human head”. In: *Optics Express* 16.20 (Sept. 29, 2008), pp. 15514–15530. ISSN: 1094-4087. DOI: 10.1364/OE.16.015514.

[32] Guoqiang Yu et al. “Time-dependent blood flow and oxygenation in human skeletal muscles measured with noninvasive near-infrared diffuse optical spectroscopies”. In: *Journal of Biomedical Optics* 10.2 (Mar. 2005), p. 024027. ISSN: 1083-3668, 1560-2281. DOI: 10.1117/1.1884603.

[33] Markus Belau et al. “Noninvasive observation of skeletal muscle contraction using near-infrared time-resolved reflectance and diffusing-wave spectroscopy”. In: *Journal of Biomedical Optics* 15.5 (Sept. 2010), p. 057007. ISSN: 1083-3668, 1560-2281. DOI: 10.1117/1.3503398.

[34] Xiaojun Cheng et al. “Measuring neuronal activity with diffuse correlation spectroscopy: a theoretical investigation”. In: *Neurophotonics* 8.3 (Aug. 2021), p. 035004. ISSN: 2329-423X, 2329-4248. DOI: 10.1117/1.NPh.8.3.035004.

List of Figures

List of Tables

List of Symbols

Variable	Description	SI unit
D	diffusion coefficient (Fick's law)	m
D_B	diffusion coefficient (Brownian motion)	$\mathrm{m^2\,s^{-1}}$
g	anisotropy factor	[−]
g_1	normalized first-order autocorrelation	[−]
g_1^s	normalized first-order autocorrelation (single-scattering regime)	[−]
G_1	first-order autocorrelation	$\mathrm{V^2\,m^{-2}}$
G_1^T	transport first-order autocorrelation	$\mathrm{V^2\,m^{-2}\,sr^{-1}}$
g_2	normalized second-order autocorrelation	[−]
G_2	second-order autocorrelation	$\mathrm{W^2\,m^{-4}}$
h	Planck's constant	J s
I	radiance	$\mathrm{W\,m^{-2}\,sr^{-1}}$
	optical intensity	$\mathrm{W\,m^{-2}}$
$\boldsymbol{J}$	flux vector	$\mathrm{W\,m^{-2}}$
k_0	wave number of light	$\mathrm{m^{-1}}$
k_B	Boltzmann constant	$\mathrm{J\,K^{-1}}$
ℓ_a	absorption mean free path	m
ℓ'	transport mean free path	m
ℓ_{eff}	effective attenuation length	m
n	refractive index	[−]
$\hat{\boldsymbol{n}}$	normal unit vector	[−]
p	scattering phase function	[−]
q_0	isotropic source term	$\mathrm{W\,m^{-3}}$
Q_0	isotropic source amplitude	J
$\boldsymbol{q_1}$	directional source term	$\mathrm{W\,m^{-3}}$
r	radial coordinate	m
	radius of a particle	m

$\langle \Delta r^2 \rangle$	mean-square displacement of moving scatterers	m^2
$\boldsymbol{r}$	position vector	m
R	reflectance	$\mathrm{W\,m^{-2}}$
R_{eff}	effective Fresnel reflectance	[–]
$\hat{\boldsymbol{s}}$	direction unit vector	[–]
t	time	s
$\mathrm{d}t$	unit time	s
T	absolute temperature	K
U	photon density	$\mathrm{m^{-3}}$
v	speed of light	$\mathrm{m\,s^{-1}}$
$\mathrm{d}V$	unit volume	m^3
z	depth coordinate	m
z_0	source depth	m
z_b	extrapolated boundary	m
z_s	extrapolated source depth	m
α	fraction of moving scatterers	[–]
β	Siegert relation parameter	[–]
ε	radiative source term	$\mathrm{W\,m^{-3}\,sr^{-1}}$
η	dynamic viscosity	$\mathrm{kg\,m^{-1}\,s^{-1}}$
θ	scattering angle	rad
λ	optical wavelength	m
μ_a	absorption coefficient	$\mathrm{m^{-1}}$
μ_s	scattering coefficient	$\mathrm{m^{-1}}$
μ_s'	reduced scattering coefficient	$\mathrm{m^{-1}}$
ν	optical frequency	Hz
ρ_a	volumetric density of absorbers	$\mathrm{m^{-3}}$
ρ_s	volumetric density of scatterers	$\mathrm{m^{-3}}$
σ_a	absorption cross section	m^2
σ_s	scattering cross section	m^2
$\mathrm{d}\Sigma$	unit surface area	m^2
τ	time delay	s
Φ	fluence	$\mathrm{W\,m^{-2}}$
$\mathrm{d}\Omega$	unit solid angle	sr